nature cell biology

Microtubule-associated proteins control the kinetics of microtubule nucleation

Michal Wieczorek[1], Susanne Bechstedt[1], Sami Chaaban[1] and Gary J. Brouhard[1,2]

Microtubules are born and reborn continuously, even during quiescence. These polymers are nucleated from templates, namely γ-tubulin ring complexes (γ-TuRCs) and severed microtubule ends. Using single-molecule biophysics, we show that nucleation from γ-TuRCs, axonemes and seed microtubules requires tubulin concentrations that lie well above the critical concentration. We measured considerable time lags between the arrival of tubulin and the onset of steady-state elongation. Microtubule-associated proteins (MAPs) alter these time lags. Catastrophe factors (MCAK and EB1) inhibited nucleation, whereas a polymerase (XMAP215) and an anti-catastrophe factor (TPX2) promoted nucleation. We observed similar phenomena in cells. We conclude that GTP hydrolysis inhibits microtubule nucleation by destabilizing the nascent plus ends required for persistent elongation. Our results explain how MAPs establish the spatial and temporal profile of microtubule nucleation.

Microtubule nucleation is the process by which soluble αβ-tubulin subunits are first converted into a growing microtubule. Spontaneous nucleation, or the process by which microtubules form *de novo* from free tubulin subunits, is a kinetically unfavourable, multi-step process[1]. Consequently, microtubule nucleation in cells occurs from templates, either the γ-TuRC (refs 2,3) or the severed end of a pre-existing microtubule[4–6]. The γ-TuRC is a conical oligomer[7] in which 13 γ-tubulins are arranged into a ring by γ-tubulin complex proteins (reviewed in ref. 8). Microtubules elongate from the γ-TuRC at centrosomes[9] or at non-centrosomal sites[10]. Microtubules are also nucleated by templates formed by microtubule severing. The severing pathway is prominent, for example, in the establishment of cortical microtubule arrays in *Arabidopsis thaliana*[6] and in neurons[11]. Templates are thought to preform nuclei, such that microtubule growth is no longer limited by a kinetically unfavourable, multi-step process[8].

An open question is how the rate of microtubule nucleation is regulated in space and time. The rate of nucleation increases significantly as cells enter mitosis[12], and the spatial profile of nucleation is peaked in the centre of the *Xenopus laevis* spindle[13]. A prominent hypothesis for how these nucleation profiles are established is that nucleation is regulated by factors that attach the γ-TuRC to other cellular structures[14] and activate nucleation[8]. Alternatively, nucleation may be regulated by MAPs (ref. 15). For example, centrosomes placed in *X. laevis* egg extracts depleted of XMAP215, a processive microtubule polymerase[16,17], have a reduced microtubule density[18]. Reducing the activity of XMAP215 in *X. laevis* spindles with point mutations, however, did not change spindle length in a manner consistent with a reduced nucleation rate[19]. Thus, it remains unclear whether XMAP215 participates in nucleation. Conversely, MAPs may inhibit nucleation from centrosomes; increasing the levels of stathmin, a microtubule catastrophe factor[20], reduced the rate of centrosomal nucleation in mouse embryonic fibroblasts[21].

MAPs are also implicated in the nucleation of microtubules in the vicinity of chromatin[22], which generates a Ran–GTP gradient on nuclear envelope breakdown[23]. This gradient releases 'spindle assembly factors' from importin-β, notably the MAP TPX2 (ref. 24). RNA-mediated interference of TPX2 in HeLa cells caused a breakdown in spindle formation[25], a result attributed specifically to defects in chromatin-mediated nucleation. The microtubules nucleated with the help of TPX2 recruit additional γ-TuRCs through augmin[26], giving rise to local amplification of microtubule number. This 'branching nucleation' was reconstituted in *X. laevis* egg extracts[27], and addition of recombinant TPX2 or a dominant-active Ran substantially increased the number of nucleation events. TPX2 also nucleates microtubules in purified tubulin solutions[28], however, suggesting that it may act as an independent nucleation factor.

What is missing is a framework for understanding the role of MAPs in microtubule nucleation. If attached and activated γ-TuRCs make nucleation fast and easy, how could a MAP increase the rate of nucleation? Here, we have developed a single-molecule assay that allows us to observe the initiation of microtubule growth from nucleation templates. We discovered that nucleation from templates is itself a kinetically unfavourable process that is limited by the formation of a plus end capable of persistent growth. We demonstrate that MAPs

[1]McGill University, Department of Biology, 1205 ave Docteur Penfield, Montréal, Québec H3A 1B1, Canada.
[2]Correspondence should be addressed to G.J.B. (e-mail: gary.brouhard@mcgill.ca)

Received 4 November 2014; accepted 14 May 2015; published online 22 June 2015; DOI: 10.1038/ncb3188

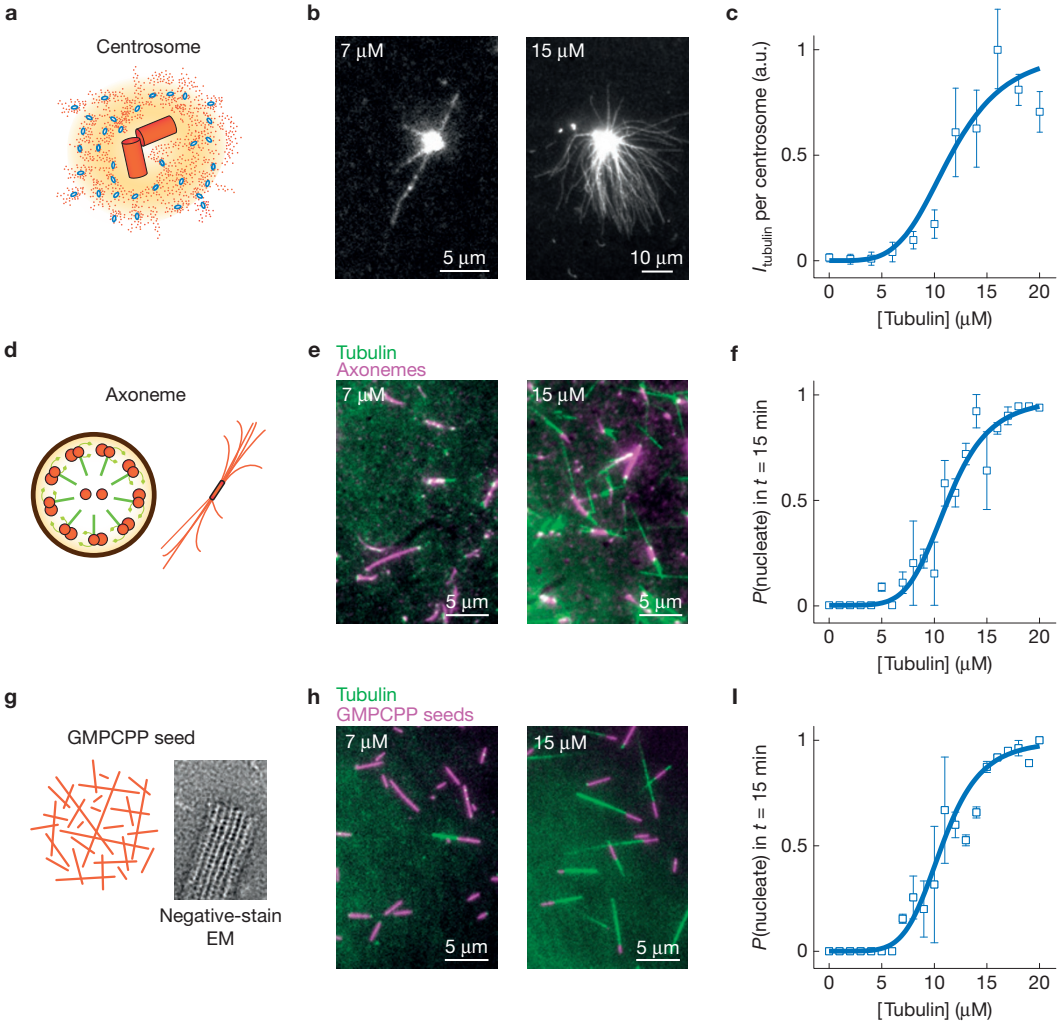

Figure 1 Microtubule nucleation from templates is a sigmoid function of tubulin concentration. (**a**) Schematic of a centrosome. The centrioles (orange cylinders) are surrounded by γ-TuRCs (blue rings) and the pericentriolar material (small orange spots). (**b**) Images of microtubules grown from centrosomes at 7 μM tubulin (left) and 15 μM tubulin (right). (**c**) Plot of the normalized tubulin fluorescence intensity around each centrosome. Centrosomes were identified by γ-tubulin immunofluorescence (Supplementary Fig. 1B). For increasing tubulin concentrations, $n = 18$, 25, 18, 38, 53, 35, 35, 37, 24, 18 and 27 centrosomes, respectively. Data were pooled across 2–4 experiments. (**d**) Schematic of an axoneme. Left: cross-sectional view showing 9 microtubule doublets surrounding a central pair; right: microtubules growing from an axoneme fragment. (**e**) Total internal reflection micrographs of microtubules (green) produced by axonemes (magenta) at 7 μM tubulin (left) and 15 μM tubulin (right). (**f**) Plot of the percentage of axonemes that produced at least one microtubule within the 15 min experiment. For increasing tubulin concentrations, $n = 15$, 30, 30, 30, 30, 34, 31, 37, 30, 32, 38, 33, 30, 28, 37, 28, 31, 38, 36, 18 and 16 axonemes, respectively. Data were pooled across 1–2 experiments. (**g**) Schematic of microtubule seeds grown in the presence of GMPCPP (left), and a representative negative-stain electron micrograph (right) confirming that our seeds present a blunt, ring-shaped surface. (**h**) Total internal reflection micrographs of microtubules (green) produced by GMPCPP seeds (magenta) at 7 μM tubulin (left) and 15 μM tubulin (right). (**i**) Plot of the percentage of GMPCPP seeds that produced a microtubule within the 15 min experiment. For increasing tubulin concentrations, $n = 15$, 25, 22, 29, 25, 35, 40, 44, 64, 50, 50, 70, 66, 50, 52, 51, 41, 42, 46, 20 and 20 GMPCPP seeds, respectively. Data were pooled across 1–4 experiments Solid lines in **c**,**f** and **i** are fits to a sigmoid curve of the form $y(x) = x^s/(C + x^s)$. All error bars represent s.e.m.

can significantly influence the kinetics of this process, acting either as nucleation-promoting or nucleation-inhibiting factors. Our results explain the conflicting data on the role of MAPs in microtubule nucleation and complement the attachment and activation model.

RESULTS

Microtubule nucleation is limited by a kinetic barrier

We began by revisiting the classic 1984 experiments on nucleation from centrosomes[29]. We incubated centrosomes, a source of γ-TuRCs (Fig. 1a and Supplementary Fig. 1A,B), with varying concentrations of fluorescent tubulin for $t = 15$ min and pelleted them onto coverslips. At 7 μM tubulin, we observed very few microtubules, whereas at 15 μM tubulin many microtubules were observed in a typical microtubule 'aster' (Fig. 1b). The intensity of the tubulin signal around the centrosome increased sigmoidally with increasing tubulin concentrations (Fig. 1c). The results overlaid the 1984 data reasonably well (Supplementary Fig. 1C). Next, we repeated the 1988 experiments on nucleation from axonemes[30]. We adhered axonemes (Fig. 1d) to the

surface of a flow chamber and introduced increasing concentrations of fluorescent tubulin. At 7 μM tubulin, very few axonemes produced microtubules, whereas at 15 μM tubulin most axonemes have produced at least one microtubule (Fig. 1e). The probability that an axoneme produced a microtubule in $t = 15$ min at each tubulin concentration (hereafter, the nucleation probability curve) is a sigmoid response (Fig. 1f) that also overlaid the 1988 data (Supplementary Fig. 1D). We fitted our data to a sigmoidal function and noted similar fit parameters (for centrosomes, the tubulin concentration for half-maximal nucleation $C = 11.6 \pm 0.7$ μM, and the steepness of the response $s = 4.3 \pm 1.1$; for axonemes, $C = 11.4 \pm 0.3$ μM, $s = 5.3 \pm 0.7$).

To obtain well-defined templates that produce single microtubules, we chose the ends of GMPCPP microtubules, another commonly used nucleation template whose blunt surface mimics the end of a severed microtubule (Fig. 1g). We adhered GMPCPP seeds to the surface of a flow chamber and introduced increasing concentrations of fluorescent tubulin (Fig. 1h and Supplementary Video 1). The nucleation probability curve (Fig. 1i) is a sigmoid response with similar parameters to the centrosomes and axonemes ($C = 10.7 \pm 0.2$ μM, $s = 5.75 \pm 1.0$). Our three nucleation templates have several differences: γ-TuRCs have a γ-tubulin binding surface[7], whereas axonemes and GMPCPP seeds present a β-tubulin surface[31]; GMPCPP seeds have a 14-protofilament structure[32], whereas γ-TuRCs have a 13-protofilament structure[33]. Nevertheless, the three templates performed with similar fit parameters.

The common sigmoid response may indicate that there is a finite probability for a template to produce a microtubule within a given time interval and that this probability increases with tubulin concentration. The alternative hypothesis is that the templates that do not fire quickly at low tubulin concentrations are 'damaged' or inactivated. To test this alternative, we exposed a set of GMPCPP seeds to 10 μM tubulin in two consecutive experiments (Supplementary Fig. 1E). If some seeds are inactive, then the same subset of active seeds should fire twice. We observed that only 7% of our seeds fired twice. The expected value from two independent experiments was 8% ($E[P_{regrow}] = P_1 \times P_2$; we measured $P_1 = 33\%$ and $P_2 = 25\%$, so $E[P_{regrow}] = 8\%$). We conclude that microtubule nucleation from our templates is stochastic. Our results indicate that templates face a kinetic barrier: a minimum tubulin concentration (~6 μM) is required before the nucleation probability becomes measurable.

Initiation of microtubule growth differs significantly from persistent elongation

It is important to make a distinction between the concentration required for a template to fire and the 'critical concentration', C_c, of microtubule polymerization. C_c is defined classically (and simplistically[34]) as $C_c = k_{off}/k_{on}$, where k_{on} is the apparent association rate constant and k_{off} is the dissociation rate constant[35] (Fig. 2a,b). To determine C_c, we measured microtubule growth rates as a function of tubulin concentration and fitted the results to a line (Fig. 2a), as many others have done[36,37]. An extrapolation of this fit gives $C_c = 1.3 \pm 0.4$ μM. The C_c predicts measurable growth rates between 1 and 5 μM tubulin, but these measurements are missing because the seeds do not nucleate (Fig. 2a). We predicted that if the kinetic barrier to nucleation could be overcome, microtubule growth would be observable in this range.

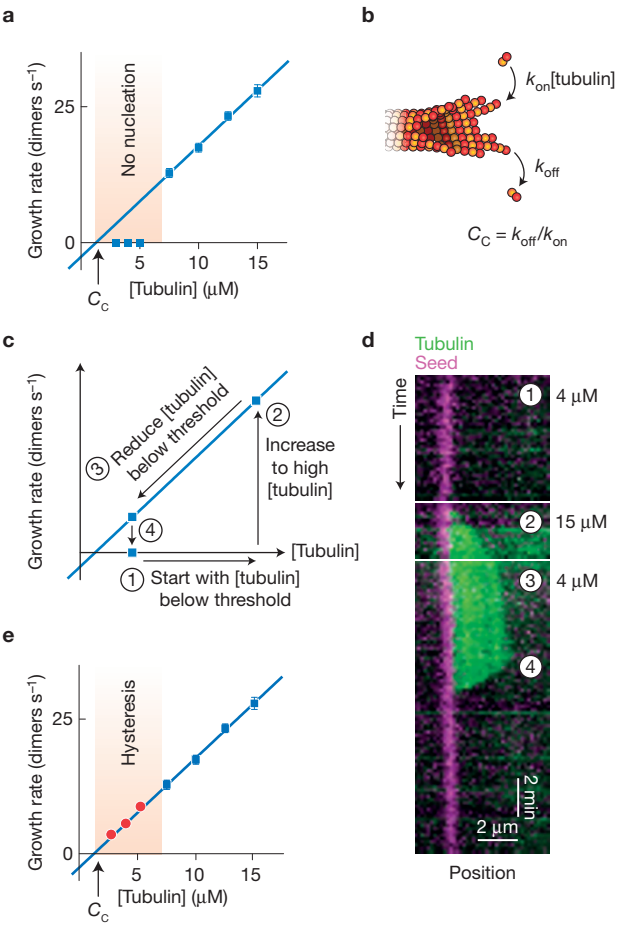

Figure 2 Microtubule plus ends elongate at tubulin concentrations where templates do not. (**a**) Plot of microtubule growth rate as a function of tubulin concentration. No growth is observed between the critical concentration for microtubule polymerization ($C_c \approx 1$ μM) and ~6 μM (faded red zone). The blue line is a weighted line of best fit to the data. For increasing tubulin concentrations, $n = 18$, 20, 18 and 13 growing microtubules, respectively. Data were pooled across 3 independent experiments. (**b**) Schematic of a polymerizing microtubule end demonstrating the relationship between the on-rate constant, k_{on}, the off-rate constant, k_{off}, and C_c. (**c**) Schematic of an experiment designed to circumvent the apparent barrier to nucleation. (1) Seeds are incubated in sub-threshold tubulin concentrations; (2) the seeds are then nucleated with a high probability using a tubulin concentration well above the threshold for nucleation; (3) once microtubules have nucleated, the tubulin concentration is brought back below the threshold and imaging continues. (4) These slowly growing microtubules eventually undergo catastrophe and the seeds are no longer able to elongate. (**d**) Kymograph showing the results of an experiment performed according to **c**. (**e**) Plot of the microtubule growth rate as a function of tubulin concentration from **a** (blue squares and corresponding fit) populated with growth rates measured below the nucleation threshold (red circles). For increasing tubulin concentrations, $n = 7$, 10 and 12 growing microtubules, respectively. Data were pooled over 2–3 experiments. All error bars represent s.e.m.

To test this prediction, we incubated GMPCPP seeds with 4 μM tubulin, a concentration at which elongation is predicted but not observed (Fig. 2d, panel 1). The solution was exchanged with 15 μM tubulin, a concentration at which GMPCPP seeds quickly produce growing microtubules (Fig. 2d, panel 2). We then exchanged the solution back to 4 μM tubulin (see Supplementary Fig. 2A for data confirming solution exchange). Despite the mechanical strain and

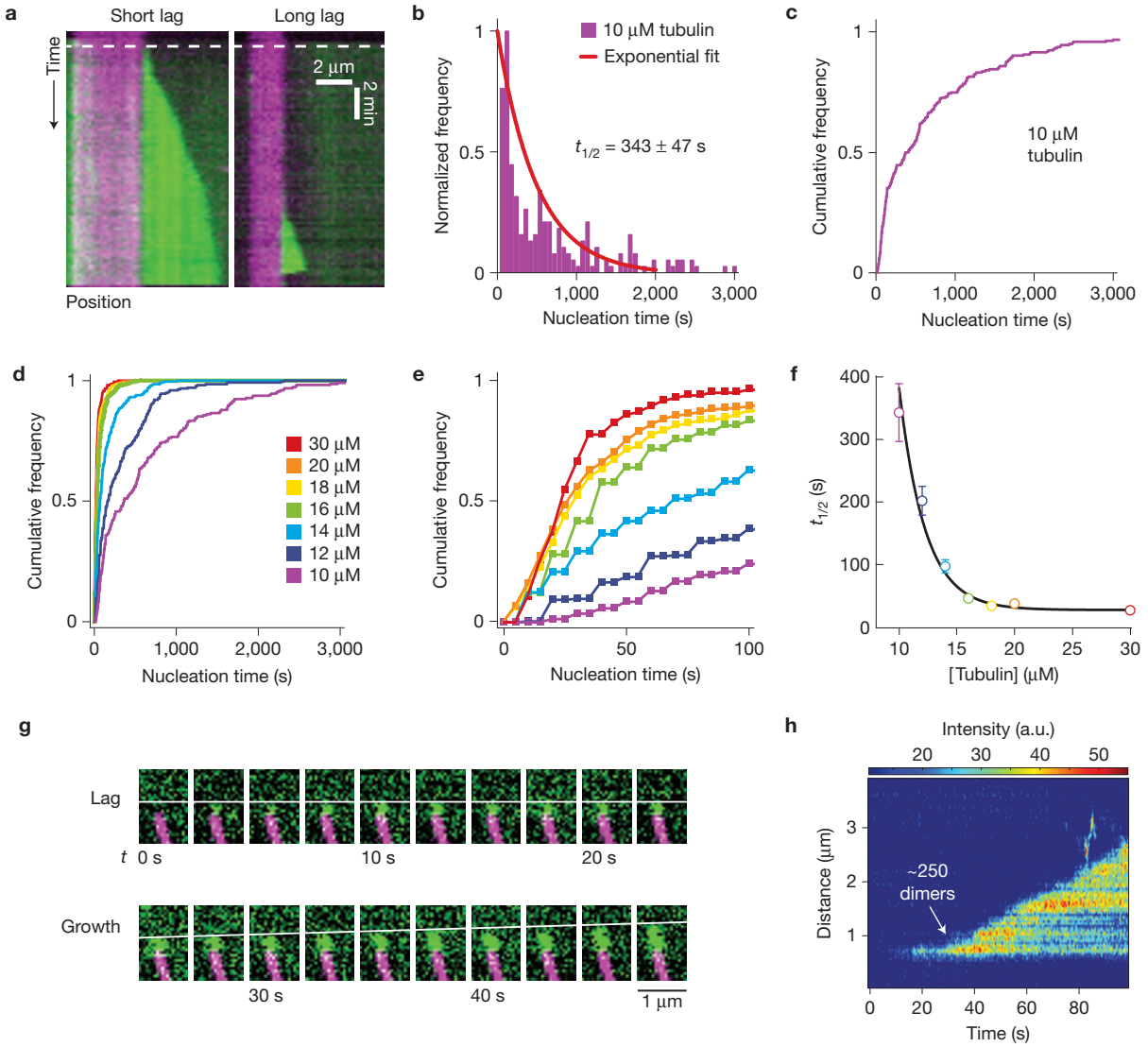

Figure 3 There is a time lag associated with templated nucleation. (**a**) Kymographs depicting short nucleation times (left) and long nucleation times (right) from GMPCPP seeds in a 10 μM tubulin solution. The white dashed line represents the start of the experiment, as determined by tracking the background tubulin fluorescence (Supplementary Fig. 3B). (**b**) Histogram of the time lag until steady-state elongation at 10 μM tubulin. The red line is a fit of the first 2,000 s to an exponential distribution (see Methods). n=223 GMPCPP seeds from different experiments. (**c**) Plot of the cumulative frequency distribution from the data in **b**. (**d**) Plots of the cumulative frequency distributions at increasing tubulin concentrations. For increasing tubulin concentrations, n = 223, 277, 281, 310, 336, 367 and 218 GMPCPP seeds, respectively from different experiments. (**e**) Zoom-in on the first 100 seconds of these cumulative frequency plots. (**f**) Characteristic half-times, or $t_{1/2}$, of the unbinned, normalized data in **d** obtained from fits to exponential distributions, as in **b**. Error bars represent the propagated upper and lower 95% confidence intervals produced from the fits. The solid black line is an exponential decay fit of the form $y(x) = y_0 + ae^{-kx}$, where x is the tubulin concentration. (**g**) Still series showing tubulin (green) arriving at the end of a GMPCPP microtubule seed (magenta). For the first ~20 s, the tubulin signal is stationary (top series, white line), after which elongation occurs (bottom series, white line). (**h**) Heat-mapped kymograph of the tubulin signal at the end of a GMPCPP seed. From $t \approx$ 20–30 s, a tubulin signal is detectable. Elongation begins at $t \approx$ 30 s. On the basis of an analysis of fluorescence intensities (see Methods), we estimate that at least 250 dimers are present when elongation occurs (n=312 nucleation events from different experiments).

damage that solution exchange will cause, microtubules continued to elongate for $\langle t \rangle = 2.7 \pm 1.7$ min at the growth rate predicted by our fit (Fig. 2d, panel 3, predicted rate: 6.0 ± 0.3 dimers s^{-1}; measured rate: 6.0 ± 0.4 dimers s^{-1}). After catastrophe occurred, the GMPCPP seed did not grow again (Fig. 2d, panel 4). In other words, the plot of microtubule growth rate versus tubulin concentration shows hysteresis. This procedure (Fig. 2d and Supplementary Video 2) allowed us to populate the plot of growth rate versus tubulin concentration in the previously inaccessible concentration range (Fig. 2e).

Our results demonstrate a difference between the events that lead to the production of a plus end by a template and the continued elongation of this plus end. Elongation can occur at tubulin concentrations where nucleation cannot. Therefore, the concentration required to initiate elongation (~6 μM) differs from the critical concentration (~1 μM), as well as the concentration required for

spontaneous nucleation, which is >20 μM in the absence of glycerol[1] (Supplementary Fig. 2B–E).

The time to nucleate a plus end falls sharply with increasing tubulin concentration

We have observed that templated nucleation, like spontaneous nucleation, is kinetically unfavourable. We therefore examined how long it typically takes to nucleate GMPCPP seeds. At 10 μM tubulin, we observed that every seed does, in fact, nucleate if given sufficient time. Many seeds experience a short time lag before nucleation occurs (Fig. 3a, left), while others experience longer time lags (Fig. 3a, right). Importantly, if the same seeds were nucleated twice, their time lags were uncorrelated (Supplementary Fig. 3A). We plotted the distribution of 'nucleation times' (Fig. 3b) as a cumulative frequency distribution (Fig. 3c). As a simple model, we fitted the data to an exponential distribution, which gave us a characteristic half-time of $t_{1/2} = 343 \pm 47$ s for 10 μM tubulin (Fig. 3b). Increasing the tubulin concentration made nucleation faster (Fig. 3d,e) and decreased the $t_{1/2}$ in an exponential manner (Fig. 3f). It is interesting to note that an extrapolation of this exponential fit to 2.5 μM tubulin gives $t_{1/2} = 170$ min, which is an order of magnitude longer than a typical experiment (15 min, Fig. 1). Additionally, $t_{1/2}$ extrapolates to 27 ± 4 s at infinite tubulin concentrations, which is significantly longer than the time required for our channels to reach 95% buffer exchange (4.0 ± 0.1 s, Supplementary Fig. 3B) or 95% temperature equilibration (17 ± 4.2 s, Supplementary Fig. 3C). In addition, at high time resolution, we saw initial fluorescent tubulin signals that preceded elongation by many seconds (Fig. 3g). Analysis of these signals revealed that, on average, ~250 dimers are present when steady-state elongation begins (Fig. 3h).

Depolymerases and catastrophe factors slow down templated nucleation

We reasoned that long nucleation time lags are caused by the struggle against microtubule catastrophes in the early steps of nucleation. In other words, tubulin must self-assemble into an assembly competent plus end quickly enough that a catastrophe does not tear down the nascent structure.

If this is the case, then catastrophe factors should increase the time lags associated with templated nucleation. We tested this prediction with MCAK, a microtubule depolymerase[38] that significantly increases the catastrophe frequency[39]. We measured the nucleation probability curve in the presence of 10 nM recombinant MCAK (Supplementary Fig. 4A), a concentration sufficient to depolymerize microtubules[40] (Supplementary Fig. 4B). The curve shifted rightward significantly (Fig. 4a, $C = 16.1 \pm 0.1$ μM, $s = 13.5 \pm 1.1$), indicating that MCAK made nucleation more difficult. We also measured nucleation times, as in Fig. 3, at 12 μM tubulin plus 5 nM MCAK (Fig. 4b). The cumulative frequency distribution was shifted significantly downward, and it was not possible to nucleate 100% of the seeds during the experiment.

We also tested EB1, a microtubule end-binding protein that is concentrated at centrosomes[12,41] and is a catastrophe factor *in vitro*[42] (Supplementary Fig. 4D). At high concentrations (~1 μM), EB1 promotes spontaneous nucleation[43], perhaps owing to lattice binding. In our hands, end-tracking concentrations (200 nM) of EB1 inhibited templated nucleation, causing a significant rightward shift

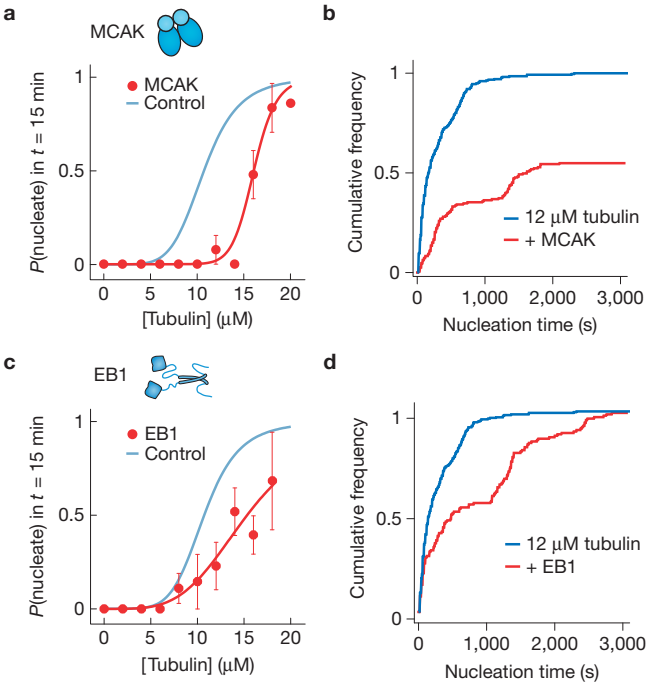

Figure 4 Catastrophe factors slow down templated nucleation. (**a**) Schematic of full-length MCAK (top). Plot of the nucleation probability curve with 10 nM MCAK (bottom). The solid red line is the sigmoidal equation fit. The faint blue line is the fit from control experiments without added MAPs (see Fig. 1i). For increasing tubulin concentrations, $n = 10$, 10, 15, 19, 15, 32, 28, 41, 47, 48 and 29 GMPCPP seeds, respectively. Data were pooled across 1–3 experiments. (**b**) Cumulative frequency distribution of the nucleation times at 12 μM tubulin represented as a cumulative frequency in the presence (red curve; $n = 106$ GMPCPP seeds from different experiments) or absence (blue curve) of 5 nM MCAK. (**c**) Schematic of the full-length EB1 (top). Plot of the nucleation probability curve with 200 nM EB1 (bottom). The solid red line is the sigmoidal equation fit. The faint blue line is the fit from control experiments without added MAPs (see Fig. 1i). For increasing tubulin concentrations, $n = 10$, 15, 28, 24, 46, 43, 47, 49, 52 and 47 GMPCPP seeds, respectively. Data were pooled across 1–3 experiments. (**d**) Cumulative frequency distribution of the nucleation times at 12 μM tubulin in the presence (red curve; $n = 140$ GMPCPP seeds from different experiments) or absence (blue curve) of 200 nM EB1. All error bars represent s.e.m.

in the nucleation probability curve (Fig. 4c, $C = 15.3 \pm 0.5$ μM, $s = 4.0 \pm 0.7$) and increasing nucleation times at 12 μM tubulin (Fig. 4d, $t_{1/2} = 445 \pm 80$ s versus $t_{1/2} = 202 \pm 24$ s). This result persisted even when we suppressed the lattice binding of EB1 by adding salt (Supplementary Fig. 4E,F). Our results demonstrate that catastrophes slow down microtubule nucleation and that MCAK and EB1 act as nucleation-inhibiting factors.

Anti-catastrophe factors and polymerases accelerate templated nucleation

As catastrophe factors inhibited templated nucleation, we predicted that polymerases and anti-catastrophe factors would accelerate nucleation by either protecting nascent structures from catastrophe or building the plus end faster. TPX2 is a candidate for a MAP that accelerates nucleation from the augmin–γ-TuRC complexes in the chromatin-mediated nucleation pathway[27,44]. The effects of TPX2 on microtubule dynamics are not known. We purified recombinant human TPX2 from insect cells (Fig. 5a). In dynamic microtubule

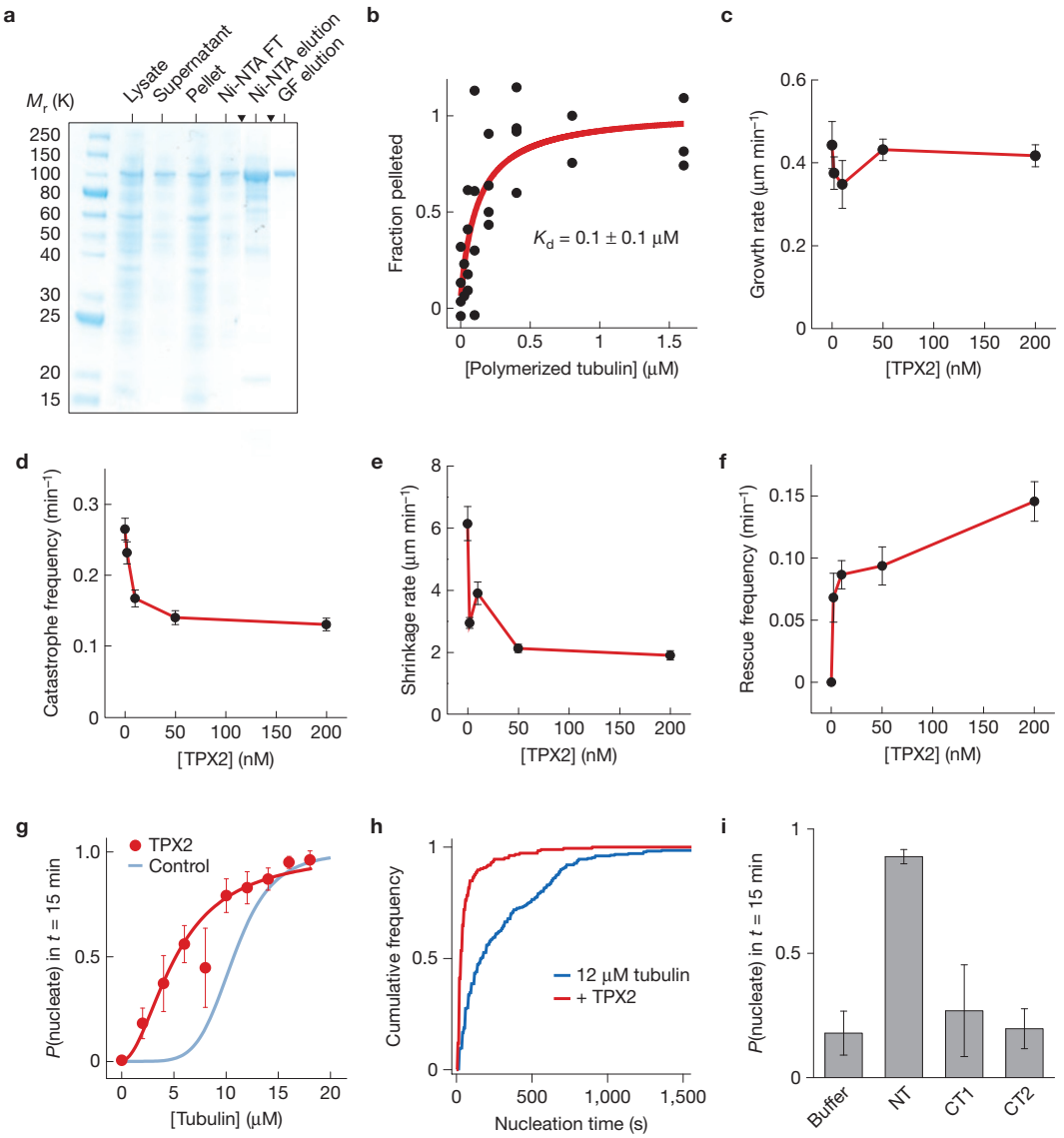

Figure 5 TPX2 is an anti-catastrophe factor that accelerates nucleation. (**a**) Coomassie-stained SDS–PAGE gel of the TPX2 purification. From left to right: crude lysate, clarified supernatant, insoluble pellet, Ni-NTA column flow through (FT), Ni-NTA column elution fractions, and final gel filtration (GF) column elution. Solid triangles indicate positions where the lanes have been cropped from the same original gel (Supplementary Fig. 7). (**b**) Plot of the TPX2 fraction that pelleted with microtubules measured from SDS–PAGE gels (Supplementary Fig. 5A). The red line is a fit to a hyperbolic function of the form $y(x)=A+(B-A)x/(k+x)$, which was used to calculate a K_d of $0.1\pm0.1\,\mu M$. For increasing tubulin concentrations, $n=4$, 2, 4, 4, 4, 4, 4, 2 and 3 independent experiments. (**c**) Plot of microtubule growth rates at 8 μM tubulin against TPX2 concentration. For increasing TPX2 concentrations, $n=20$, 48, 39, 37 and 40 microtubules, respectively; data pooled across 2 experiments. (**d**) Plot of the catastrophe frequency at 8 μM tubulin against TPX2 concentration. For increasing TPX2 concentrations, $n=20$, 48, 39, 37 and 40 events, respectively; data pooled across 2 experiments. (**e**) Plot of the post-catastrophe shrinkage rate at 8 μM tubulin against TPX2 concentration. For increasing TPX2 concentrations, $n=12$, 40, 14, 13 and 26 microtubules, respectively; data pooled across 2 experiments. (**f**) Plot of the rescue frequency (number of observed rescues divided by the total time the microtubules spent shrinking) at 8 μM tubulin against TPX2 concentration. For increasing TPX2 concentrations, $n=12$, 4, 11, 14 and 10 events, respectively; data pooled across 2 experiments. (**g**) Plot of the nucleation probability curve with 200 nM TPX2. Solid red line, sigmoidal equation fit. Faint blue line, fit from control experiments without added MAPs (see Fig. 1i). For increasing tubulin concentrations, $n=15$, 193, 165, 143, 151, 142, 174, 145, 166 and 100 GMPCPP seeds, respectively; data pooled across 1–3 experiments. (**h**) Cumulative frequency distribution of the nucleation times at 12 μM tubulin represented as a cumulative frequency in the presence (red curve; $n=185$ nucleation events from different experiments) or absence (blue curve) of 200 nM TPX2. (**i**) Plot of the nucleation probability at 8 μM tubulin in the presence of TPX2 truncation constructs NT, CT1 or CT2. For each condition, $n=438$, 443, 348 and 182 GMPCPP seeds, respectively; data pooled across 3 experiments. Error bars, s.e.m.

assays, TPX2 had no measurable effect on microtubule growth rates at 8 μM tubulin (Fig. 5c). Rather, TPX2 reduced the catastrophe frequency (Fig. 5d), decreased the rate of post-catastrophe shrinkage (Fig. 5e), and increased the rescue frequency (Fig. 5f). TPX2 strongly promoted nucleation, enabling us to observe microtubule elongation at tubulin concentrations close to the critical concentration

(Fig. 5g, $C = 5.2 \pm 0.1\,\mu M$, $s = 1.9 \pm 0.1$). TPX2 also made nucleation significantly faster than in control conditions (Fig. 5h; $t_{1/2} = 50 \pm 7$ s). These effects depended on an amino-terminal region of TPX2 that binds to microtubules[45] (Fig. 5b,i and Supplementary Fig. 5B,C).

Next, we tested XMAP215, a processive microtubule polymerase[16,17] that increases the growth rate of microtubules by five- to tenfold (Supplementary Fig. 5D,E). We found that XMAP215 caused a leftward shift in the nucleation probability curve, indicating that it makes microtubule nucleation easier (Fig. 6a, $C = 8.9 \pm 0.4\,\mu M$, $s = 3.7 \pm 0.8$). XMAP215 also made GMPCPP seeds nucleate microtubules faster (Fig. 6b; $t_{1/2} = 78 \pm 10$ s). We note that kinesin-1, a motor protein with no obvious effect on microtubule dynamics, did not affect nucleation (Supplementary Fig. 5F). These results demonstrate that TPX2 and XMAP215 act as nucleation-promoting factors by accelerating the formation of plus ends and protecting them from catastrophe.

Given the strong effects of MCAK and TPX2 on nucleation, we predicted that the absence of catastrophes would eliminate the nucleation barrier entirely. We therefore tested GMPCPP–tubulin, which does not undergo catastrophe yet has similar association and dissociation rate constants to GTP–tubulin[46]. GMPCPP–tubulin rapidly nucleated from GMPCPP seeds (Fig. 6c; $C = 0.14 \pm 0.01\,\mu M$, $s = 1.4 \pm 0.2$). The characteristic half-time was $t_{1/2} = 23 \pm 4.6$ s at 1 μM GMPCPP–tubulin (Fig. 6d), which is similar to the $t_{1/2}$ at 30 μM GTP–tubulin. Taken together, these results indicate that GTP hydrolysis inhibits microtubule nucleation by causing catastrophes that destabilize the nascent plus ends required for persistent elongation.

Depletion of tubulin by nocodazole inhibits microtubule nucleation in cells

Our *in vitro* results predict that the nucleation rate in cells should drop sharply as the concentration of tubulin is reduced. To test this idea, we measured centrosomal nucleation rates in cell lines expressing fluorescently tagged EBs (Supplementary Fig. 6F and Supplementary Video 3), as described previously[4,12]. We added increasing amounts of nocodazole, a drug that competes for the colchicine site[47] and sequesters tubulin into an inactive state[48]. Small concentrations of nocodazole caused a significant decrease in the rate of nucleation (Fig. 7a,b and Supplementary Video 4). EB comet velocities also decreased with nocodazole titration (Supplementary Fig. 6A). We plotted the nucleation rate against the comet velocity and fitted the data to a line (Fig. 7c); the fit shows that nucleation ceases at a point where microtubule growth is still robust (x-intercept $= 5.1 \pm 4.0\,\mu m\,min^{-1}$), analogous to our *in vitro* data (Fig. 7d). We observed similar results with colchicine, another tubulin-sequestering drug (Supplementary Fig. 6D). As a control, we showed that nocodazole and colchicine themselves do not interfere with end-tracking by EB1–GFP *in vitro* (Supplementary Fig. 6E).

These results argue that a kinetic barrier to nucleation exists *in vivo*. Low doses of nocodazole are known to perturb microtubule dynamics in cells[49], which may be due to the fact that the 'infinite' bath of nocodazole in the media sequesters more than equimolar amounts of tubulin. Supplementary Fig. 6B shows the amount of tubulin sequestered by 0.2 μM nocodazole as a function of the nocodazole-tubulin affinity, and Supplementary Fig. 6C shows a corresponding theoretical plot of the nucleation rate against tubulin concentration *in vivo*. Although the precise mechanism of nocodazole remains undetermined, our results

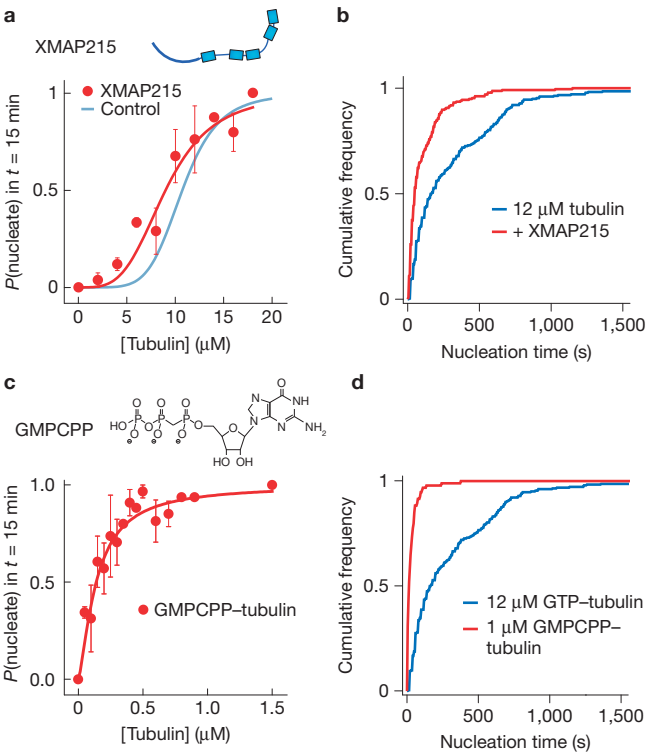

Figure 6 A polymerase and GMPCPP–tubulin both accelerate nucleation. (**a**) Schematic drawing of full-length XMAP215 (top). Plot of the nucleation probability curve with 200 nM XMAP215 (bottom). The solid red line is the sigmoidal equation fit. The faint blue line is the fit from control experiments without added MAPs (see Fig. 1i). For increasing tubulin concentrations, $n = 15$, 52, 50, 48, 55, 46, 32, 16, 49 and 24 GMPCPP seeds, respectively; data pooled across 1–3 experiments. (**b**) Cumulative frequency distribution of the nucleation times at 12 μM tubulin in the presence (red curve; $n = 235$ GMPCPP seeds from different experiments) or absence (blue curve) of 200 nM XMAP215. (**c**) Schematic drawing of GMPCPP (top). Plot of the probability that a GMPCPP seed produces a GMPCPP microtubule in 15 min (bottom). The solid red line is the sigmoidal equation fit. For increasing tubulin concentrations, $n = 15$, 84, 32, 38, 49, 38, 45, 35, 48, 17, 33, 30, 26, 16, 16 and 12 GMPCPP seeds , respectively; data pooled across 1–5 experiments. (**d**) Cumulative frequency distribution of the nucleation times at 1 μM GMPCPP–tubulin (red curve; $n = 95$ GMPCPP seeds from different experiments) or at 12 μM GTP–tubulin (blue curve). All error bars represent s.e.m.

demonstrate a sharp reduction in microtubule nucleation rates from a small perturbation in the effective tubulin concentration.

DISCUSSION

Our reconstitution of microtubule nucleation events has enabled us to discover that templated nucleation is associated with a significant time lag, indicative of a kinetically unfavourable, multi-step process. The unfavourable kinetics of templated nucleation provide a framework for understanding the role of MAPs as nucleation-promoting or nucleation-inhibiting factors. More precisely, the local activity of tubulin and MAPs will determine the time lag for nucleation. This concept may reconcile the conflicting data on the role of XMAP215 in nucleation. In intact *X. laevis* spindles, nucleation may be accelerated by other MAPs, such that reduced XMAP215 activity is inconsequential[19], whereas in other extract conditions[18], the local environment near the centrosomes enabled the observation of an

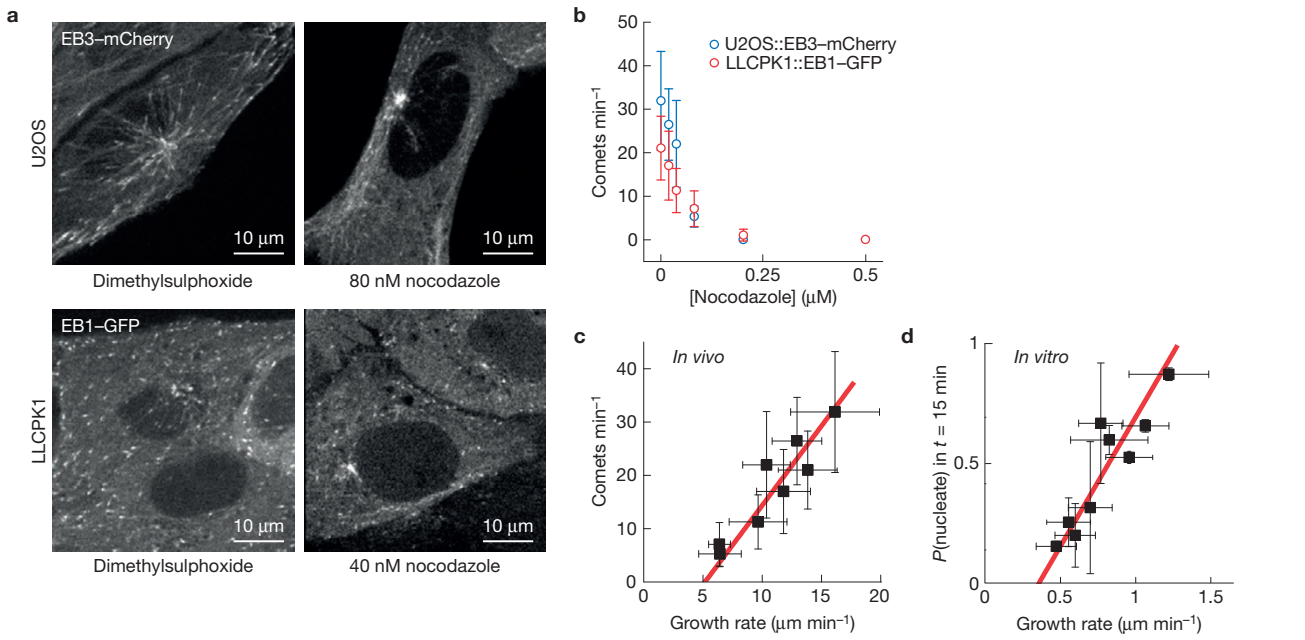

Figure 7 Depletion of tubulin by nocodazole reduces the rate of nucleation in cells. (**a**) Images of cells expressing fluorescently tagged EB3 (U2OS, top) or EB1 (LLCPK1, bottom) in the presence (right) or absence (left) of added nocodazole. (**b**) Plot of the number of comets that emerged from the centrosome per minute at increasing nocodazole concentrations. For increasing nocodazole concentrations, $n=12$, 7, 14, 9 and 8 U2OS cells, and 29, 15, 19, 8, 23 and 6 LLCPK1 cells, respectively; data pooled across 2 experiments. Error bars represent s.d. (**c**) Plot of the number of comets that emerged from the centrosome per minute from **b** as a function of the corresponding microtubule growth rates (Supplementary Fig. 6A). The red line is a linear fit taking into account both *x* and *y* errors. (**d**) Nucleation probability curve from Fig. 1i plotted as a function of the corresponding microtubule growth rates. For the corresponding increasing tubulin concentrations, $n=18$, 31, 20, 47, 21, 21, 18, 13 and 18 microtubules, respectively; data pooled across 3 experiments. The red line is a linear fit taking into account both *x* and *y* errors. Error bars represent s.e.m.

effect. Similarly, in the environment surrounding chromatin, where the rate of nucleation is peaked[13], the release of TPX2 from importin-β will enable augmin–γ-TuRC complexes to nucleate quickly. We note that MCAK is inactivated at the centromere by the kinase aurora B (ref. 50). TPX2 activation and MCAK inactivation will create an environment around chromatin in which the kinetic barrier to nucleation is significantly reduced. In these ways, the local MAP environment will contribute to the spatial and temporal profile of nucleation.

Our model for the role of MAPs complements the ongoing work on the regulation of nucleation by attachment and activation[8]. In early reconstitutions of the *Saccharomyces cerevisiae* γ-TuRC, its nucleation activity was low relative to the expectation from centrosomes[51]. In the cryo-electron microscopy structures of the γ-tubulin small complex[52] and a recombinant γ-TuRC expressed with a fragment of Spc110 (ref. 7), the arrangement of γ-tubulins was cracked open relative to the 13-protofilament microtubule. Forcing the γ-TuRC to form a closed ring by cysteine crosslinking caused a two- to threefold increase in the number of microtubules formed[53]. It has been proposed that proteins could close the γ-TuRC ring, thereby activating nucleation[8]. In mammalian cells, a strong candidate is Cdk5Rap2, which contains a domain referred to as the γ-tubulin nucleation activator[54]. It is our hope that the framework we have developed will be useful for characterizing the effect of attachment and activation on the kinetics of nucleation.

We speculate that the kinetic barrier to templated nucleation is partly the consequence of a structural mismatch between the tapered, outwardly curved, and flattened 'sheets' at microtubule plus ends[55,56] and the blunt, ring-shaped templates on which they are built. The binding of tubulin subunits to a sheet versus a blunt template could differ in many ways. The strength of the lateral bond may depend on the angle with which one tubulin subunit contacts its neighbour[57]. Lateral bonds may also change as tubulin straightens during polymerization[58]. In addition, the strength of the longitudinal bond between tubulin subunits may depend on its curvature. The exchangeable nucleotide binding site is situated directly at the longitudinal interface, and thus the curvature at this interface could alter the rate of GTP hydrolysis. We anticipate that adaptation of mathematical models[59] or computational models[60] will be instrumental in testing hypotheses of this type.

It has recently been demonstrated that catastrophes are caused by an ageing process, wherein microtubules accumulate 'defects' and thus become more likely to undergo catastrophes[39]. At first glance, our results suggest the opposite: the catastrophe frequency is very high on nascent plus ends but drops precipitously once a growing plus end has emerged. It may be that nascent plus ends contain many 'defects'. Resolving these defects may lead to 'birth' and the onset of steady-state elongation. Once elongation commences, the microtubule ages, until a catastrophe causes it to shrink back to its template, from which it is only later reborn. □

METHODS

Methods and any associated references are available in the online version of the paper.

Note: Supplementary Information is available in the online version of the paper

ACKNOWLEDGEMENTS

We thank H. Higgs for suggesting the hysteresis experiment (Fig. 2) during the question period of an American Society for Cell Biology mini-symposium. We thank L. Cassimeris (Lehigh University, USA) for providing the LLCPK1:EB1–GFP cell line, A. Bird (Max Planck Institute of Molecular Physiology, Germany) for providing the U2OS:EB3–mCherry cell line, and R. Ohi (Vanderbilt University, USA) for providing the LLCPK1:GFP–tubulin cell line. We thank the Cell Imaging and Analysis Network for microscopy support. We thank C. Rocha for help with immunoblot sample preparation. We thank A. Bird, C. Friel, J. Howard, L. Rice and M. Zanic for comments on the manuscript. This work was supported by the Canadian Institutes of Health Research (CIHR, MOP-111265 to G.J.B.), by the Natural Sciences and Engineering Research Council of Canada (NSERC, no. 372593-09 to G.J.B.), and by McGill University. M.W. is supported by an NSERC CGS-D award and a Fonds de Recherche du Quebec—Nature et Technologie Bourse de Doctorat en Recherche. S.C. is supported by the NSERC CREATE training program in the Cellular Dynamics of Macromolecular Complexes and an NSERC CGS-D. G. Brouhard is a CIHR New Investigator.

AUTHOR CONTRIBUTIONS

M.W., S.B. and G.J.B. conceived the project. M.W. performed nucleation experiments, characterized the MAPs, and imaged cells. S.B. established infrastructure for molecular biology and protein expression. S.C. performed electron microscopy experiments. M.W. and G.J.B. analysed data, developed models, and wrote the paper.

COMPETING FINANCIAL INTERESTS

The authors declare no competing financial interests.

Published online at http://dx.doi.org/10.1038/ncb3188

Reprints and permissions information is available online at www.nature.com/reprints

1. Voter, W. A. & Erickson, H. P. The kinetics of microtubule assembly. Evidence for a two-stage nucleation mechanism. *J. Biol. Chem.* **259,** 10430–10438 (1984).
2. Zheng, Y., Wong, M. L., Alberts, B. & Mitchison, T. Nucleation of microtubule assembly by a γ-tubulin-containing ring complex. *Nature* **378,** 578–583 (1995).
3. Moritz, M., Braunfeld, M. B., Sedat, J. W., Alberts, B. & Agard, D. A. Microtubule nucleation by γ-tubulin-containing rings in the centrosome. *Nature* **378,** 638–640 (1995).
4. Srayko, M., Kaya, A., Stamford, J. & Hyman, A. A. Identification and characterization of factors required for microtubule growth and nucleation in the early *C. elegans* embryo. *Dev. Cell.* **9,** 223–236 (2005).
5. McNally, K., Audhya, A., Oegema, K. & McNally, F. J. Katanin controls mitotic and meiotic spindle length. *J. Cell Biol.* **175,** 881–891 (2006).
6. Lindeboom, J. J. *et al.* A mechanism for reorientation of cortical microtubule arrays driven by microtubule severing. *Science* **342,** 1245533 (2013).
7. Kollman, J. M., Polka, J. K., Zelter, A., Davis, T. N. & Agard, D. A. Microtubule nucleating γ-TuSC assembles structures with 13-fold microtubule-like symmetry. *Nature* **466,** 879–882 (2010).
8. Kollman, J. M., Merdes, A., Mourey, L. & Agard, D. A. Microtubule nucleation by γ-tubulin complexes. *Nat. Rev. Mol. Cell Biol.* **12,** 709–721 (2011).
9. Oakley, B. R., Oakley, C. E., Yoon, Y. & Jung, M. K. γ-tubulin is a component of the spindle pole body that is essential for microtubule function in Aspergillus nidulans. *Cell* **61,** 1289–1301 (1990).
10. Luders, J. & Stearns, T. Microtubule-organizing centres: a re-evaluation. *Nat. Rev. Mol. Cell Biol.* **8,** 161–167 (2007).
11. Baas, P. W. & Ahmad, F. J. The plus ends of stable microtubules are the exclusive nucleating structures for microtubules in the axon. *J. Cell Biol.* **116,** 1231–1241 (1992).
12. Piehl, M., Tulu, U. S., Wadsworth, P. & Cassimeris, L. Centrosome maturation: measurement of microtubule nucleation throughout the cell cycle by using GFP-tagged EB1. *Proc. Natl Acad. Sci. USA* **101,** 1584–1588 (2004).
13. Brugues, J., Nuzzo, V., Mazur, E. & Needleman, D. J. Nucleation and transport organize microtubules in metaphase spindles. *Cell* **149,** 554–564 (2012).
14. Luders, J., Patel, U. K. & Stearns, T. GCP-WD is a γ-tubulin targeting factor required for centrosomal and chromatin-mediated microtubule nucleation. *Nat. Cell Biol.* **8,** 137–147 (2006).
15. Bre, M. H. & Karsenti, E. Effects of brain microtubule-associated proteins on microtubule dynamics and the nucleating activity of centrosomes. *Cell Motil. Cytoskeleton* **15,** 88–98 (1990).
16. Gard, D. L. & Kirschner, M. W. A microtubule-associated protein from Xenopus eggs that specifically promotes assembly at the plus-end. *J. Cell Biol.* **105,** 2203–2215 (1987).
17. Brouhard, G. J. *et al.* XMAP215 is a processive microtubule polymerase. *Cell* **132,** 79–88 (2008).
18. Popov, A. V., Severin, F. & Karsenti, E. XMAP215 is required for the microtubule-nucleating activity of centrosomes. *Curr. Biol.* **12,** 1326–1330 (2002).
19. Reber, S. B. *et al.* XMAP215 activity sets spindle length by controlling the total mass of spindle microtubules. *Nat. Cell Biol.* **15,** 1116–1122 (2013).
20. Belmont, L. D. & Mitchison, T. J. Identification of a protein that interacts with tubulin dimers and increases the catastrophe rate of microtubules. *Cell* **84,** 623–631 (1996).
21. Ringhoff, D. N. & Cassimeris, L. Stathmin regulates centrosomal nucleation of microtubules and tubulin dimer/polymer partitioning. *Mol. Biol. Cell* **20,** 3451–3458 (2009).
22. Heald, R. *et al.* Self-organization of microtubules into bipolar spindles around artificial chromosomes in *Xenopus* egg extracts. *Nature* **382,** 420–425 (1996).
23. Carazo-Salas, R. E. *et al.* Generation of GTP-bound Ran by RCC1 is required for chromatin-induced mitotic spindle formation. *Nature* **400,** 178–181 (1999).
24. Wittmann, T., Boleti, H., Antony, C., Karsenti, E. & Vernos, I. Localization of the kinesin-like protein Xklp2 to spindle poles requires a leucine zipper, a microtubule-associated protein, and dynein. *J. Cell Biol.* **143,** 673–685 (1998).
25. Gruss, O. J. *et al.* Chromosome-induced microtubule assembly mediated by TPX2 is required for spindle formation in HeLa cells. *Nat. Cell Biol.* **4,** 871–879 (2002).
26. Goshima, G., Mayer, M., Zhang, N., Stuurman, N. & Vale, R. D. Augmin: a protein complex required for centrosome-independent microtubule generation within the spindle. *J. Cell Biol.* **181,** 421–429 (2008).
27. Petry, S., Groen, A. C., Ishihara, K., Mitchison, T. J. & Vale, R. D. Branching microtubule nucleation in Xenopus egg extracts mediated by augmin and TPX2. *Cell* **152,** 768–777 (2013).
28. Schatz, C. A. *et al.* Importin α-regulated nucleation of microtubules by TPX2. *EMBO J.* **22,** 2060–2070 (2003).
29. Mitchison, T. & Kirschner, M. Microtubule assembly nucleated by isolated centrosomes. *Nature* **312,** 232–237 (1984).
30. Walker, R. A. *et al.* Dynamic instability of individual microtubules analyzed by video light microscopy: rate constants and transition frequencies. *J. Cell Biol.* **107,** 1437–1448 (1988).
31. Mitchison, T. J. Localization of an exchangeable GTP binding site at the plus end of microtubules. *Science* **261,** 1044–1047 (1993).
32. Meurer-Grob, P., Kasparian, J. & Wade, R. H. Microtubule structure at improved resolution. *Biochemistry* **40,** 8000–8008 (2001).
33. Moritz, M., Braunfeld, M. B., Guenebaut, V., Heuser, J. & Agard, D. A. Structure of the γ-tubulin ring complex: a template for microtubule nucleation. *Nat. Cell Biol.* **2,** 365–370 (2000).
34. Gardner, M. K. *et al.* Rapid microtubule self-assembly kinetics. *Cell* **146,** 582–592 (2011).
35. Oosawa, F. & Asakura, S. *Thermodynamics of the Polymerization of Protein* Vol. 20 (Academic Press, 1975).
36. Mitchison, T. & Kirschner, M. Dynamic instability of microtubule growth. *Nature* **312,** 237–242 (1984).
37. Drechsel, D. N., Hyman, A. A., Cobb, M. H. & Kirschner, M. W. Modulation of the dynamic instability of tubulin assembly by the microtubule-associated protein tau. *Mol. Biol. Cell* **3,** 1141–1154 (1992).
38. Hunter, A. W. *et al.* The kinesin-related protein MCAK is a microtubule depolymerase that forms an ATP-hydrolyzing complex at microtubule ends. *Mol. Cell* **11,** 445–457 (2003).
39. Gardner, M. K., Zanic, M., Gell, C., Bormuth, V. & Howard, J. Depolymerizing kinesins Kip3 and MCAK shape cellular microtubule architecture by differential control of catastrophe. *Cell* **147,** 1092–1103 (2011).
40. Helenius, J., Brouhard, G., Kalaidzidis, Y., Diez, S. & Howard, J. The depolymerizing kinesin MCAK uses lattice diffusion to rapidly target microtubule ends. *Nature* **441,** 115–119 (2006).
41. Askham, J. M., Vaughan, K. T., Goodson, H. V. & Morrison, E. E. Evidence that an interaction between EB1 and p150(Glued) is required for the formation and maintenance of a radial microtubule array anchored at the centrosome. *Mol. Biol. Cell* **13,** 3627–3645 (2002).
42. Bieling, P. *et al.* Reconstitution of a microtubule plus-end tracking system *in vitro*. *Nature* **450,** 1100–1105 (2007).
43. Vitre, B. *et al.* EB1 regulates microtubule dynamics and tubulin sheet closure *in vitro*. *Nat. Cell Biol.* **10,** 415–421 (2008).
44. Gruss, O. J. *et al.* Ran induces spindle assembly by reversing the inhibitory effect of importin α on TPX2 activity. *Cell* **104,** 83–93 (2001).
45. Brunet, S. *et al.* Characterization of the TPX2 domains involved in microtubule nucleation and spindle assembly in Xenopus egg extracts. *Mol. Biol. Cell* **15,** 5318–5328 (2004).
46. Hyman, A. A., Salser, S., Drechsel, D. N., Unwin, N. & Mitchison, T. J. Role of GTP hydrolysis in microtubule dynamics: information from a slowly hydrolyzable analogue, GMPCPP. *Mol. Biol. Cell* **3,** 1155–1167 (1992).
47. Hoebeke, J., Nijen, G. V. & Brabander, M. D. Interaction of oncodazole (r 17934), a new anti-tumoral drug, with rat brain tubulin. *Biochem. Biophys. Res. Commun.* **69,** 319–324 (1976).
48. Head, J., Lee, L. L., Field, D. J. & Lee, J. C. Equilibrium and rapid kinetic studies on nocodazole-tubulin interaction. *J. Biol. Chem.* **260,** 11060–11066 (1985).
49. Vasquez, R. J., Howell, B., Yvon, A. M., Wadsworth, P. & Cassimeris, L. Nanomolar concentrations of nocodazole alter microtubule dynamic instability *in vivo* and *in vitro*. *Mol. Biol. Cell* **8,** 973–985 (1997).
50. Andrews, P. D. *et al.* Aurora B regulates MCAK at the mitotic centromere. *Dev. Cell.* **6,** 253–268 (2004).
51. Vinh, D. B., Kern, J. W., Hancock, W. O., Howard, J. & Davis, T. N. Reconstitution and characterization of budding yeast γ-tubulin complex. *Mol. Biol. Cell* **13,** 1144–1157 (2002).
52. Kollman, J. M. *et al.* The structure of the γ-tubulin small complex: implications of its architecture and flexibility for microtubule nucleation. *Mol. Biol. Cell* **19,** 207–215 (2008).

53. Kollman, J. M. *et al.* Ring closure activates yeast γ-turc for species-specific microtubule nucleation. *Nat. Struct. Mol. Biol.* **22,** 132–137 (2015).
54. Choi, Y. K., Liu, P., Sze, S. K., Dai, C. & Qi, R. Z. CDK5RAP2 stimulates microtubule nucleation by the γ-tubulin ring complex. *J. Cell Biol.* **191,** 1089–1095 (2010).
55. Chretien, D., Fuller, S. D. & Karsenti, E. Structure of growing microtubule ends: two-dimensional sheets close into tubes at variable rates. *J. Cell Biol.* **129,** 1311–1328 (1995).
56. Bechstedt, S., Lu, K. & Brouhard, G. J. Doublecortin recognizes the longitudinal curvature of the microtubule end and lattice. *Curr. Biol.* **24,** 2366–2375 (2014).
57. Wang, H. W. & Nogales, E. Nucleotide-dependent bending flexibility of tubulin regulates microtubule assembly. *Nature* **435,** 911–915 (2005).
58. Rice, L. M., Montabana, E. A. & Agard, D. A. The lattice as allosteric effector: structural studies of αβ- and γ-tubulin clarify the role of GTP in microtubule assembly. *Proc. Natl Acad. Sci. USA* **105,** 5378–5383 (2008).
59. Janosi, I. M., Chretien, D. & Flyvbjerg, H. Modeling elastic properties of microtubule tips and walls. *Eur. Biophys. J.* **27,** 501–513 (1998).
60. VanBuren, V., Cassimeris, L. & Odde, D. J. Mechanochemical model of microtubule structure and self-assembly kinetics. *Biophys. J.* **89,** 2911–2926 (2005).

METHODS

Tubulin, microtubule, axoneme and centrosome preparations. Tubulin was purified from juvenile bovine brains using a modified version of the high-PIPES method[61], wherein the first polymerization cycle was performed in 100 mM PIPES instead of 1 M PIPES. Labelling of tubulin with tetramethylrhodamine (TAMRA) and Alexa Fluor 488 succinimidyl esters (Life Technologies) was performed as described previously[62]. GMPCPP seeds were prepared by polymerizing a 1:4 molar ratio of TAMRA-labelled/unlabelled tubulin in the presence of guanosine-5′-[(α,β)-methyleno]triphosphate (GMPCPP, Jena Biosciences) in two cycles, as described previously[63]. GMPCPP seeds prepared in this way were stable for several months at −80 °C and were blunt when observed under electron microscopy after staining with 0.75% uranyl formate (Fig. 1g). Axoneme fragments were purified from *Strongylocentrotus purpuratus* sperm as described previously[64]. Centrosomes were purified from cultured CHO-K1 cells using sucrose density gradient centrifugation as described previously[29]. Centrosome-containing sucrose density gradient elution fractions were identified by immunoblotting against γ-tubulin (1:1,000 dilution of monoclonal clone GTU-88, Sigma; Supplementary Fig. 1A).

Expression and purification of MAPs. All protein purifications were performed at 4 °C using an Akta Purifier (GE Healthcare) when appropriate. The cDNA for a constitutively active rat kinesin-1–GFP ($rKin_{430}$–GFP) was a gift from R. Cross (University of Warwick, UK) to J. Howard (Yale University, USA), and was expressed and purified as described previously[62]. XMAP215 and EB1 were expressed and purified as described previously[62]. EB1–GFP was generated similarly to untagged EB1, but the PCR product was ligated in a modified pHAT vector containing an N-terminal 6xHis-tag followed by a PreScission site and a carboxy-terminal EGFP followed by a Strep-tag II (ref. 65) for affinity purification. EB1–GFP was expressed and purified just like untagged EB1, but was additionally gel-filtered over a Superdex 200 10/300 column (GE Healthcare) pre-equilibrated in the wash buffer. MCAK was expressed and purified as described previously[40] with some modifications. The initial cation exchange step was omitted, and MCAK-rich Ni-NTA fractions were directly gel-filtered over a Superdex 200 10/300 column (GE Healthcare) pre-equilibrated in storage buffer: BRB80 (80 mM PIPES-KOH, pH 6.9, 1 mM EGTA, 1 mM $MgCl_2$), 150 mM KCl, 1 mM dithiothreitol, 10 μM ATP. The coding sequence for full-length human TPX2 was PCR amplified from cDNA clone 3509275 (OpenBiosystems) using PfuX7 (ref. 66) and inserted into a modified pFastBac vector containing an N-terminal 6xHis-tag followed by a tobacco etch virus (TEV) cleavage site. TPX2 was overexpressed in Sf9 cells infected with recombinant baculovirus for 72 h. The insect cell pellet was resuspended in lysis buffer (50 mM sodium phosphate pH 8.0, 300 mM NaCl, 10% glycerol, and 1 mM 2-mercaptoethanol) and lysed in a glass dounce homogenizer. The lysate was clarified by centrifugation at 100,000*g* for 45 min and then incubated with His60 resin (Clontech) for 2 h. The resin was transferred to a gravity flow column and washed extensively with lysis buffer. TPX2 was eluted with lysis buffer containing 300 mM imidazole and the 6xHis-tag was cleaved overnight by adding TEV protease to 100 μg ml^{-1}. Protein-rich fractions were gel-filtered on a Superdex 200 10/300 column (GE Healthcare) pre-equilibrated in storage buffer (BRB80, 150 mM KCl, 1 mM dithiothreitol, 10 μM ATP). TPX2 truncation constructs were designed to include or exclude the microtubule-binding domain(s) identified for *X. laevis* TPX2 (ref. 45). An alignment between human TPX2 and *X. laevis* TPX2 was performed to identify sequences homologous to *X. laevis* TPX2 amino acids 1–480, 319–715 and 481–715. Human TPX2 amino acids 1–512, 350–747 and 513–747 were subsequently PCR amplified into a modified pHAT vector containing an N-terminal 6xHis-tag, a PreScission site and a SUMO fusion protein, followed by a C-terminal Strep-tag II. A 5′ methionine was introduced into the forward primers for both C-terminal fragments. $TPX2_{1\text{-}512}$, $TPX2_{350\text{-}747}$ and $TPX2_{513\text{-}747}$ (for simplicity, hereafter termed NT, CT1 and CT2, respectively) were expressed in BL21(DE3) overnight at 18 °C and purified identically to EB1. For all proteins, purified fractions in storage buffer were supplemented with glycerol to 10% (v/v), snap frozen in liquid nitrogen, and stored at −80 °C. Fig. 5a and Supplementary Figs 4A and 5B,D show SDS–PAGE gels confirming the purity of our protein preparations.

Total internal reflection fluorescence microscopy and preparation of microscope chambers. The microscope set-up uses a Zeiss Axiovert Z1 microscope chassis, a ×100 1.45 NA Plan-apochromat objective lens, and the Zeiss TIRF III slider. A $\lambda = 491$ nm diode-pumped solid-state laser (Cobolt) was coupled to a fibre optic cable in free space and introduced into the Zeiss slider. Epifluorescence was achieved using a PhotofluorII excitation source (89 North) with wavelength-specific filter cubes (Chroma). Images were recorded using either Andor Neo sCMOS or Andor iXon+ DV-897 EMCCD cameras. In some experiments a ×1.6 optovar was used to increase magnification. Microscope chambers were constructed using custom-machined mounts[63]. In brief, cover glass was cleaned and silanized as described previously[40]. Cover glasses (22 × 22 mm and 18 × 18 mm) were separated by two layers of double-sided tape creating a channel for the exchange of solution. Image acquisition was controlled using MetaMorph (Molecular Devices).

Seeds were adhered to silanized glass slides as described previously[65] and incubated for at least 30 min at room temperature. This incubation step allowed the seeds to depolymerize slightly and ensured blunt ends for nucleation (see Fig. 1g). On the day of each experiment, aliquots of unlabelled and Alexa Fluor 488-labelled tubulin were thawed, mixed to a 1:10 molar labelling ratio, aliquoted again, and stored in liquid nitrogen. One aliquot was thawed for each experiment to avoid inconsistencies in microtubule dynamics measurements.

Microtubule growth from GMPCPP seeds was achieved by incubating flow channels with tubulin in standard polymerization buffer: BRB80, 1 mM GTP, 0.1 mg ml^{-1} BSA, 1% 2-mercaptoethanol, 250 nM glucose oxidase, 64 nM catalase, 40 mM D-glucose. ATP was also added to 1 mM for experiments with MCAK or $rKin_{430}$-GFP; no changes in microtubule dynamics, including nucleation, were detectable under added ATP (data not shown). Assays were performed at 30.5 ± 0.5 °C; an objective heater set to 35 °C and a thermocouple connected to a thin probe (Omega) allowed us to measure temperatures directly within the channel. Time-lapse image sequences were typically acquired at 5–10 s intervals, with the following exceptions. The interval was decreased to 1 s for experiments in which we observed initial nucleation events (Fig. 3g,h). The interval was increased to 20 s for nucleation time distribution measurements that took up to 3,000 s to collect (that is, at 10 μM tubulin in Fig. 3b).

***In vitro* nucleation measurements.** Nucleation from centrosomes was performed essentially as described previously[29]. Purified centrosomes were incubated with Alexa Fluor 488-labelled tubulin at 0–30 μM in BRB80 containing 1 mM GTP for $t = 15$ min at 37 °C and then fixed with 0.25% glutaraldehyde. Fixed asters were centrifuged onto cover glass and stained for γ-tubulin (1:500 of monoclonal clone GTU-88, Sigma; Supplementary Fig. 1B). Centrosomes were unambiguously identified using the γ-tubulin signal. Nucleation was quantified by assigning a summed Alexa Fluor 488–tubulin fluorescence signal along a circle of $r = 1$ μm manually drawn with the centrosome at the centre, normalized against the summed signal found along a circle of $r = 1$ μm drawn in the background.

Nucleation from axonemes was measured essentially as described previously[30]. Axonemes were allowed to adhere nonspecifically to silanized cover glass. After washing out unbound axonemes with BRB80, standard polymerization buffer containing the indicated concentration of Alexa Fluor 488-labelled tubulin was flowed in and 15 min time lapses were recorded. Axonemes and their plus ends were unambiguously identified after each experiment by introducing a solution containing 10 nM $rKin_{430}$–GFP, 1 mM ATP and 50 μg ml^{-1} κ-casein in 1× BRB80. Nucleation was measured as the percentage of individual axonemes that grew at least one microtubule within the 15 min imaging window.

Nucleation from GMPCPP seeds was measured as described above for axonemes, except they were identified easily by their TAMRA labels. Plus ends were again identified by introducing $rKin_{430}$–GFP after each experiment. Nucleation was measured as the percentage of individual GMPCPP seeds that were observed to grow at least one microtubule extension within the 15 min imaging window. All data were fitted to the sigmoidal equation $y(x) = x^s/(C + x^s)$ using OriginPro (OriginLab).

Microtubule growth rates. Microtubule growth rates were analysed by manually fitting lines to kymographs of growing microtubules using the Kymograph and Linescan features in MetaMorph (Molecular Devices). Linear least-squares fitting to growth rate data was performed in OriginPro (OriginLab).

Spontaneous nucleation experiments. The concentration of tubulin required for the formation of microtubules in the absence of seeds was measured in two ways. A turbidity-based experiment was performed at increasing tubulin concentrations and the amount of polymerized microtubules was reported as the absorbance at 350 nm ($A_{350\,nm}$) at the end of a 60 min experiment (Supplementary Fig. 2C). Samples containing final concentrations of 1× BRB80 and 1 mM GTP were zeroed in a Cary 300 UV-Vis spectrophotometer (Agilent). All spontaneous nucleation experiments were performed at 30 °C to reflect TIRF assay conditions. At 2–5 min into the experiment the recording was paused and tubulin was added to the indicated final concentrations and mixed with pipetting as quickly as possible. Recording resumed for the remaining 60 min. Data post-tubulin addition were zeroed relative to the $A_{350\,nm}$ recorded immediately after resuming the experiment, which is shown in Supplementary Fig. 2B.

The second method was based on ref. 29 but was performed without adding microtubule seeds. Samples containing 1× BRB80, 1 mM GTP and 0.1 mg ml^{-1} casein and the indicated concentration of tubulin were incubated on ice for 5 min then at 30 °C for 60 min. These samples were then centrifuged through a cushion containing 25% glycerol in 1× BRB80, 1 mM GTP and 0.1 mg ml^{-1} casein at 100,000*g* for 15 min. Microtubule pellets were resuspended in BRB80, resolved on SDS–PAGE gels (Supplementary Fig. 2D), and bands were quantified using ImageJ

DOI: 10.1038/ncb3188

(ref. 67) using a standard made from the same tubulin aliquots loaded at 10, 5, 2.5 and 1.25 μM (Supplementary Fig. 2E).

Nucleation time measurements. To measure microtubule nucleation times, we performed the assays described in Fig. 1 with GMPCPP seeds with some modifications. First, imaging was started before tubulin was introduced in the channel. Tubulin at the indicated concentration in standard polymerization buffer was flowed in and the background intensity was analysed to obtain a $t = 0$ time point, which was defined as the point at which the background intensity plateaued (Supplementary Fig. 3B). At lower tubulin concentrations, or in the presence of catastrophe factors such as MCAK and EB1, we noticed that all growing microtubules had undergone catastrophe after ~20 min and failed to re-nucleate. In other words, the flow channel 'dies' after a certain time. To obtain nucleation time data up to one hour, which was necessary for every seed to nucleate at 10 μM tubulin, for example, we devised a quasi-continuous flow experiment. After imaging for ~7.5–10 min in the initial tubulin solution, we introduced a fresh solution of tubulin to replace the 'dying' one. We repeated this several times until an imaging time of at least one hour was reached. Nucleation times were measured by logging the time frame in which an observable growing microtubule signal emerged from the end of a seed. The initially defined $t = 0$ time frame was then subtracted to obtain a nucleation time. The first 2,000 s of these nucleation time distributions were fitted to an equation of the form $y(t) = e^{-\mu t}$ (Fig. 3b), from which it follows that $t_{1/2} = \mu \ln 2$. The effects of replenishing the tubulin solution to rescue a dying channel are evident in the step-like shapes of the cumulative distributions for MCAK and EB1 (Fig. 4).

Estimate of the number of tubulin dimers at the onset of microtubule elongation. A custom MATLAB (MathWorks) script was written to estimate the number of dimers present at the onset of elongation when imaging early nucleation events (Fig. 3g,h). Briefly, the script compares the brightness of fluorescent tubulin at the onset of growth with the brightness of a defined length of the lattice with a known number of tubulin dimers. The script takes manually generated line scans of newly growing microtubules as an input. After background subtraction, smoothing, differentiation and thresholding, the nucleated microtubule is identified and the growing end is tracked using previously described methods[68]. We defined the onset of elongation ($t = t_i$) by fitting the steady-state elongation to a line and extrapolating back to the onset (arrow, Fig. 3h). The number of tubulin dimers present at the onset is estimated by $N_{Tb} \approx 813 \times \Sigma I_i / \Sigma I_{ii}$, where ΣI_i and ΣI_{ii} are the integrated fluorescence intensities at $t = t_i$ and $t = t_{ii}$, respectively. We define t_{ii} as the time at which the microtubule reaches a length of 0.5 μm and we assume ~1,625 dimers per 1 μm of microtubule lattice.

Microtubule cosedimentation assays. Paclitaxel-stabilized microtubules were prepared as described previously[69]. A small sample of the microtubule preparation was incubated on ice for 30 min and the polymerized tubulin concentration was determined spectrophotometrically using an extinction coefficient of $\varepsilon = 115{,}000\ M^{-1}cm^{-1}$. Full-length TPX2 (200 nM) was incubated with increasing amounts of stabilized microtubules in final volumes of 50 μl containing 1× BRB80, 1 mM paclitaxel and 0.1 mg ml^{-1} casein. After a 10 min incubation at room temperature samples were centrifuged at 50,000*g* for 10 min. Pellets were resuspended in 1× SDS–PAGE sample buffer and resolved on an SDS–PAGE gel (Supplementary Fig. 5A). A control containing the expected amount of TPX2 if 100% cosedimentation occurred was included for normalization purposes during analysis. Band intensities were quantified using ImageJ (ref. 67) and normalized to the control lane (Fig. 5b). The data were fitted to a hyperbolic function of the form $y(x) = A + (B - A)x/(k + x)$, which was then used to calculate a K_d of 0.1 ± 0.1 μM.

To determine whether microtubule binding correlated with the ability of TPX2 to promote nucleation, 200 nM of the truncation constructs including or excluding potential microtubule-binding domains was incubated with 1 μM paclitaxel-stabilized microtubules. Samples of sedimented pellets were prepared as above and were resolved on an SDS–PAGE gel (Supplementary Fig. 5C; top). An immunoblot against the 6xHis-tag (1:1,000 dilution of A00186, Genscript) was performed on the same samples to determine whether CT2 cosedimented with microtubules, as the molecular weight of this construct overlaps with that of tubulin (Supplementary Fig. 5C; bottom).

Centrosomal nucleation in cells. LLCPK1 cells expressing EB1–GFP (ref. 12) or U2OS cells expressing EB3–mCherry were seeded in DMEM lacking phenol red with 10% FBS, 10 mM HEPES, 1 mM sodium pyruvate, penicillin–streptomycin and 40 μg ml^{-1} G418 in 35 mm glass-bottomed Petri dishes (MatTek) the day before an experiment. Solutions of nocodazole and colchicine were made up in the same medium on the day of an experiment. Cells were exchanged into medium containing the appropriate concentration of nocodazole or colchicine and incubated at 37 °C for 15 or 60 min, respectively, before imaging. Control cells were exchanged into drug-free medium containing the same final concentration dimethylsulphoxide. The focal plane was adjusted to include the centrosomal source of EB comets (Fig. 7a). Images were acquired every 2 s for 2 min with an exposure time of 300 ms. Nucleation rates were measured according to the method described in ref. 4 and are reported in units of new comets emerging from the centrosome per minute (comets min^{-1}).

To ensure that these tubulin-sequestering drugs do not affect EB1 binding to microtubule ends, we tested EB1–GFP tip-tracking *in vitro* using our TIRF assay. We found that at 200 nM nocodazole and 500 nM colchicine, concentrations at which microtubule growth and templated nucleation are not severely impaired in the TIRF assay, EB1–GFP tip-tracking was unaffected (Supplementary Fig. 7E). The tubulin concentration in these experiments was 20 μM and the EB1–GFP concentration was 160 nM.

Estimate of EB1–GFP overexpression. The LLCPK1 cells[70] and LLCPK1:EB1–GFP cells were grown to confluency in 10 cm dishes and lysed by incubation in 500 μl of 2× Laemmli buffer (125 mM Tris pH 6.8, 20% (v/v) glycerol, 4% (w/v) SDS, 2 mM dithiothreitol and 0.1% (w/v) bromophenol blue) at room temperature. The LLCPK1 served as a control line lacking EB1–GFP. Samples were boiled at 95 °C for 10 min and run on an SDS–PAGE gel, and then probed with an antibody against EB1 (1:500 dilution of H-70, Santa Cruz Biotechnology) and β-tubulin (1:500 dilution of DM1A, Sigma) as a loading control. The EB1 blot shows a band at a relative molecular mass of about 55,000 in the LLCPK1:EB1–GFP cell line that is absent in the control LLCPK1 cells. We estimate EB1–GFP overexpression at ~30% relative to the endogenous level on the basis of the intensity of this band measured from two independent blots using ImageJ (ref. 67).

Repeatability of experiments. The repeatability of the representative images shown in Figs 1e,h, 2d, 3a,g,h and 7a and Supplementary Figs 1B,E, 2D and 5A is described in the statistical information found in the corresponding figure legends.

The centrosomes shown in Fig. 1b were not included in the analysis shown in Fig. 1c, but they do have a tubulin fluorescence intensity that falls within the range predicted by the fit in Fig. 1c. This observation was also reproduced several times in pilot experiments. The electron microscopy experiment in which we imaged GMPCPP seeds was repeated 3 times. Blunt ends were the most commonly observed.

The immunoblot in Supplementary Fig. 1A was performed once but repeated for every centrosome purification as a means of identifying positive fractions.

The background fluorescence intensity trace in Supplementary Fig. 2A was performed for several hysteresis experiments to confirm that our solution exchange was consistent between experiments.

Analysis of depolymerizing GMPCPP seeds after double-cycling with and without MCAK (Supplementary Fig. 4C) was performed once to qualitatively confirm that MCAK had no obvious effect. We confirmed this observation while performing the experiments in Fig. 4c. The experiment in which salt was added to the imaging buffer with EB1–GFP (Supplementary Fig. 4E) was performed twice.

The microtubule cosedimentation assay with TPX2 truncation constructs in Supplementary Fig. 5C was performed twice, but only one of the experiment samples was run on an α-His immunoblot.

Imaging of EB1–GFP comets on unlabelled microtubules in the presence of either nocodazole or colchicine (Supplementary Fig. 6E) was performed in three independent experiments. The immunoblot in Supplementary Fig. 6F was done twice to estimate the EB1–GFP overexpression level (see above).

61. Castoldi, M. & Popov, A. V. Purification of brain tubulin through two cycles of polymerization-depolymerization in a high-molarity buffer. *Protein Expr. Purif.* **32,** 83–88 (2003).
62. Wieczorek, M., Chaaban, S. & Brouhard, G. Macromolecular crowding pushes catalyzed microtubule growth to near the theoretical limit. *Cell. Mol. Bioeng.* **6,** 383–392 (2013).
63. Gell, C. *et al.* Microtubule dynamics reconstituted *in vitro* and imaged by single-molecule fluorescence microscopy. *Methods Cell Biol.* **95,** 221–245 (2010).
64. Waterman-Storer, C. M. Microtubule/organelle motility assays. *Curr. Protoc. Cell Biol.* Unit 13.1 (2001).
65. Bechstedt, S. & Brouhard, G. J. Doublecortin recognizes the 13-protofilament microtubule cooperatively and tracks microtubule ends. *Dev. Cell.* **23,** 181–192 (2012).
66. Norholm, M. A mutant Pfu DNA polymerase designed for advanced uracil-excision DNA engineering. *BMC Biotechnol.* **10,** 21 (2010).
67. Schneider, C. A., Rasband, W. S. & Eliceiri, K. W. NIH Image to ImageJ: 25 years of image analysis. *Nat. Methods* **9,** 671–675 (2012).
68. Demchouk, A. O., Gardner, M. K. & Odde, D. J. Microtubule tip tracking and tip structures at the nanometer scale using digital fluorescence microscopy. *Cell. Mol. Bioeng.* **4,** 192–204 (2011).
69. Noujaim, M., Bechstedt, S., Wieczorek, M. & Brouhard, G. J. Microtubules accelerate the kinase activity of aurora-b by a reduction in dimensionality. *PLoS ONE* **9,** e86786 (2014).
70. Rusan, N. M., Fagerstrom, C. J., Yvon, A. M. & Wadsworth, P. Cell cycle-dependent changes in microtubule dynamics in living cells expressing green fluorescent protein-α tubulin. *Mol. Biol. Cell* **12,** 971–980 (2001).

DOI: 10.1038/ncb3188

nature cell biology

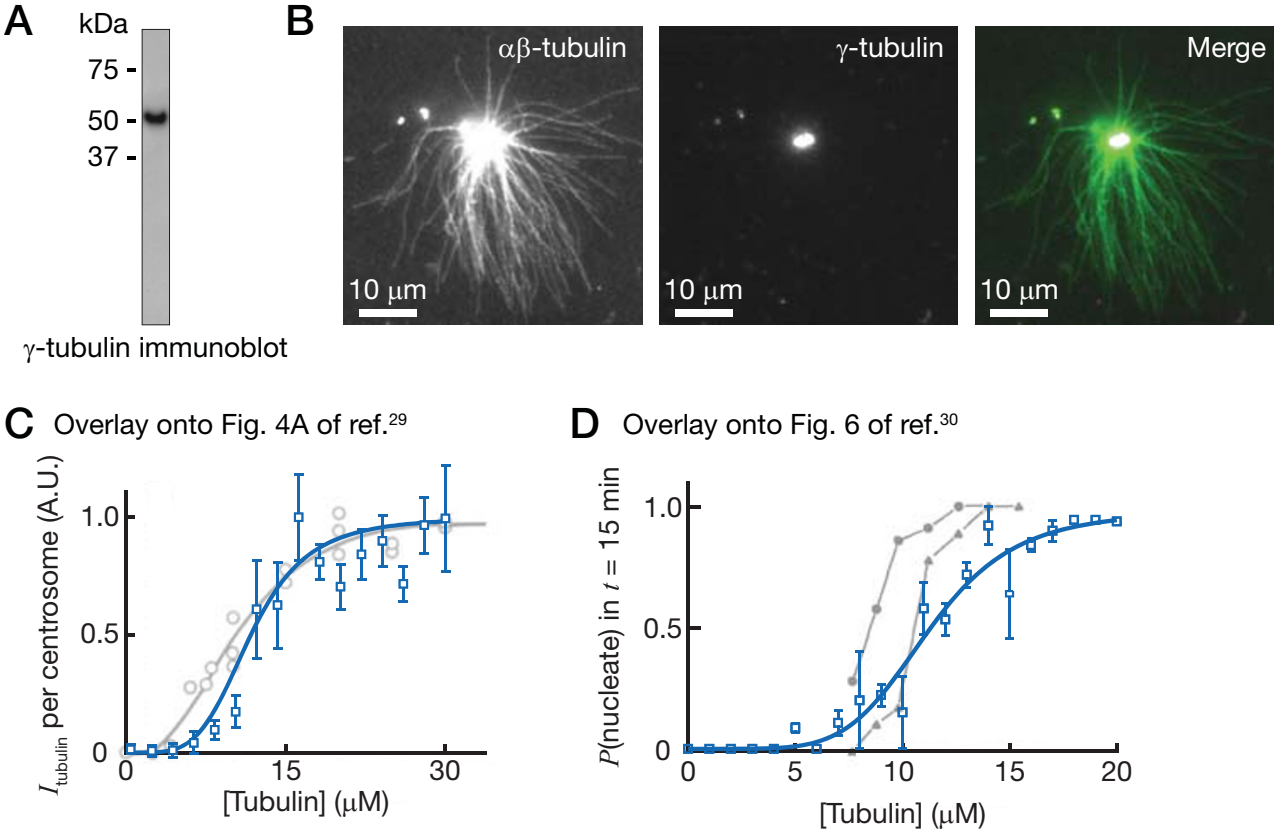

Supplementary Figure 1 Controls for centrosome, axoneme and GMPCPP nucleation experiments in Fig. 1. **(A)** Immunoblot against γ-tubulin for a purified centrosome fraction. **(B)** Immunofluorescence of purified centrosomes after microtubule nucleation showing aβ-tubulin (*left*) and γ-tubulin (middle). In the merged image (*right*), the γ-tubulin signal is at the center of the microtubule aster. **(C)** Overlay of our centrosome nucleation data (Fig. 1C) onto data from Fig. 4A of ref.[29] **(D)** Overlay of our axoneme nucleation data (Fig. 1F) onto data from Fig. 6 of ref.[30] (©1988 Walker et al. Journal of Cell Biology. 107:1437-1448. doi:10.1083/jcb.107.4.1437). **(E)** Images from two consecutive nucleation experiments performed on the same set of GMPCPP seeds. In experiment #1, 33% of the seeds produced microtubules (*left*, white arrows). In experiment #2, after thorough rinsing, 25% of the seeds produced microtubules (*right*, white arrows). The theoretical probability that a seed produced microtubules twice agrees well with the measured value (see text at right). $n = 214$ GMPCPP seeds measured consecutively in the same experiment.

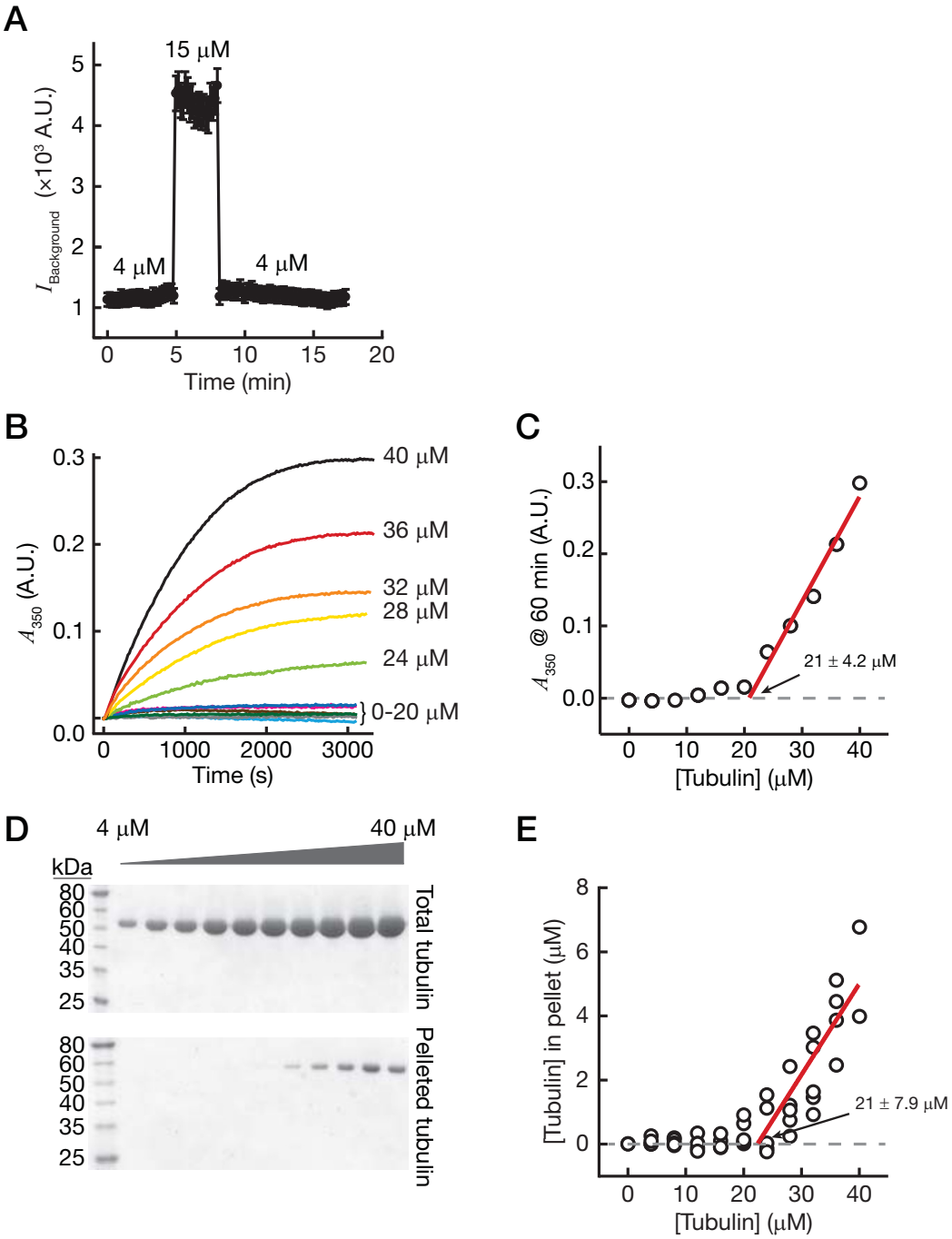

Supplementary Figure 2 Controls for hysteresis experiments in Fig. 2 and in-house spontaneous nucleation measurements. **(A)** Plot of the average background intensity from fluorescent tubulin against time for the experiment in Fig. 2D. The intensity increases when the tubulin concentration is increased from 4 μM to 15 μM. When the solution is exchanged from 15 μM back to 4 μM, the intensity returns to the baseline, 4 μM tubulin level, indicating that the solution exchange is complete. Error bars represent the s.d. of intensity values from a 20 x 20 pixel box from one experiment. **(B)** Plot of the absorbance at 350 nm (A_{350}), or turbidity, against time for solutions containing the indicated concentration of tubulin. An increase in A_{350} indicates polymer formation. **(C)** Plot of the A_{350} values at $t = 60$ min against tubulin concentration. A fit to data for which $A_{350} > 0.05$ (red line) gives an *x*-intercept of 21 ± 4.2 μM tubulin, which is the critical concentration for spontaneous nucleation. **(D)** Images of Coomassie-stained SDS-PAGE gels for the spin-down spontaneous nucleation assay, showing the total tubulin (*top gel*) and the polymeric tubulin in the pellet (*bottom gel*). **(E)** Plot of the concentration of pelleted tubulin against total tubulin concentration. A fit of the data for which the concentration of tubulin in the pellet ≥1 μM (red line) gives an *x*-intercept of 21 ± 7.9 μM. For increasing tubulin concentrations, $n = 2, 4, 5, 5, 5, 5, 5, 5, 4$ and 2 independent experiments, respectively.

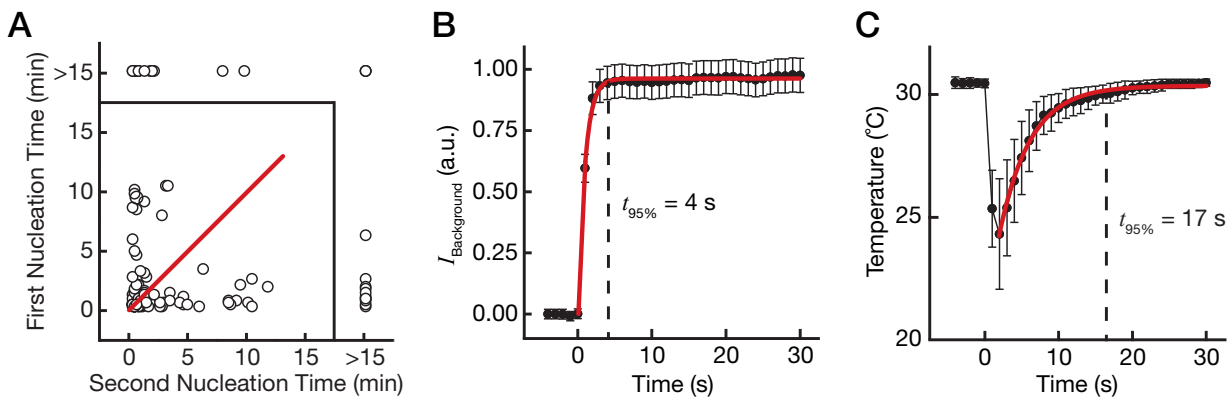

Supplementary Figure 3 Controls for nucleation time distribution experiments in Fig. 3. **(A)** Plot of the first nucleation time against the second nucleation time for two consecutive experiments in which the same set of GMPCPP seeds were exposed to 12 μM tubulin for $t = 15$ min. If a seed did not produce a microtubule during the experiment, its nucleation time was recorded as >15 min. A red line shows the result predicted by the hypothesis that the seeds will have identical nucleation times in both experiments. The data clearly do not fall on the line. $n = 118$ GMPCPP seeds. **(B)** Plot of the background intensity from fluorescent tubulin against time averaged from several experiments. The intensity increases quickly as tubulin is introduced. The red line shows a fit of the data to an exponential function, $y(t) = y_0 + ae^{kt}$. From this fit, the time at which the intensity reaches 95% of its plateau was calculated ($t_{95\%} = 4$ s, black dotted line). Error bars represent s.d. $n = 3$ independent flow-in experiments. **(C)** Plot of the flow cell temperature against time during a typical experiment. The red line is a fit of the temperature data to an exponential function, $y(t) = y_0 + ae^{kt}$. From this fit, the time at which the temperature reaches 95% of its plateau was calculated ($t_{95\%} = 17$ s, black dotted line). Error bars represent s.d. $n = 3$ independent experiments.

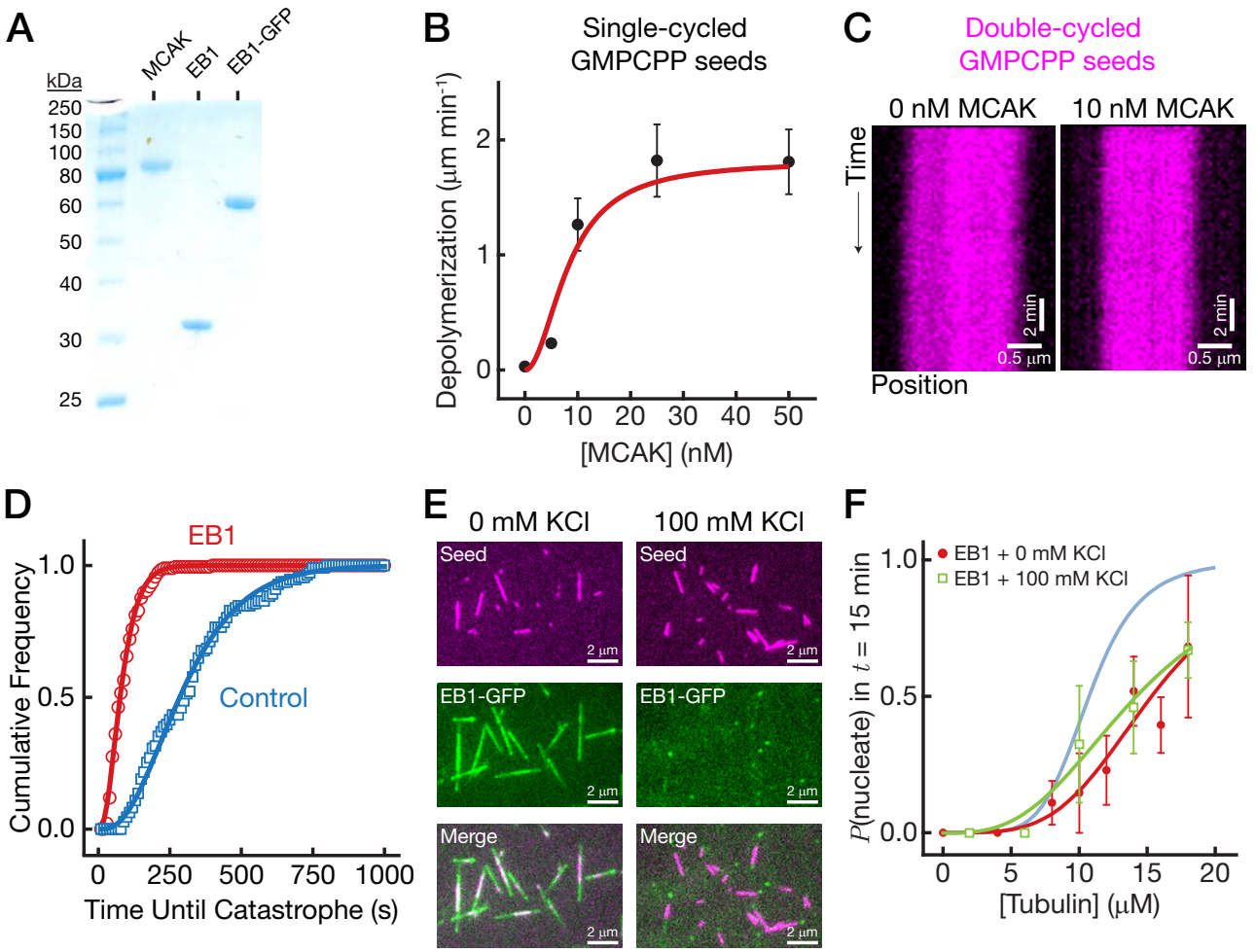

Supplementary Figure 4 Controls for the effects of MCAK and EB1 on nucleation in Fig. 4. **(A)** Image of a Coomassie-stained SDS-PAGE gel showing the purified protein fractions for MCAK, EB1, and EB1-GFP used in this study. **(B)** Plot of the depolymerization rate of GMPCPP microtubules against MCAK concentration. Error bars represent the s.d. For increasing MCAK concentrations, $n = 10$, 11, 10, 11 and 7 GMPCPP microtubules analysed in one experiment. **(C)** Kymographs showing double-cycled GMPCPP seeds used in our nucleation assays without (left) and with (right) 10 nM MCAK. Double-cycled GMPCPP seeds are resistant to depolymerization at these MCAK concentrations. **(D)** Cumulative frequency distribution of the time until catastrophe in the presence of 200 nM EB1 (*red*) and in control buffers (*blue*) at 10 μM tubulin. The solid lines are fits to the Gamma distribution, as described in Gardner et al. (2011). $n =$ 186 (with 200 nM EB1) and $n = 111$ (without EB1) catastrophe events collected from different experiments. **(E)** In the absence of added salt, EB1-GFP binds along the GMPCPP seeds, the GDP lattice and the tip of growing microtubules. Adding 100 mM KCl to the imaging solution reduces the affinity of EB1-GFP to the seed and lattice, but end-binding persists. The tubulin concentration in these experiments was 20 μM. The EB1-GFP concentration in these experiments was 200 nM. (F) In high salt conditions, EB1 still makes nucleation difficult (green squares), arguing that EB1 lattice binding does not contribute to nucleation inhibition. The solid green line is the sigmoidal equation fit. The fit from the control data is shown in light blue for comparison. For increasing tubulin concentrations, $n = 102$, 92, 105 and 140 GMPCPP seeds pooled from 3 experiments. Error bars represent s.e.m.

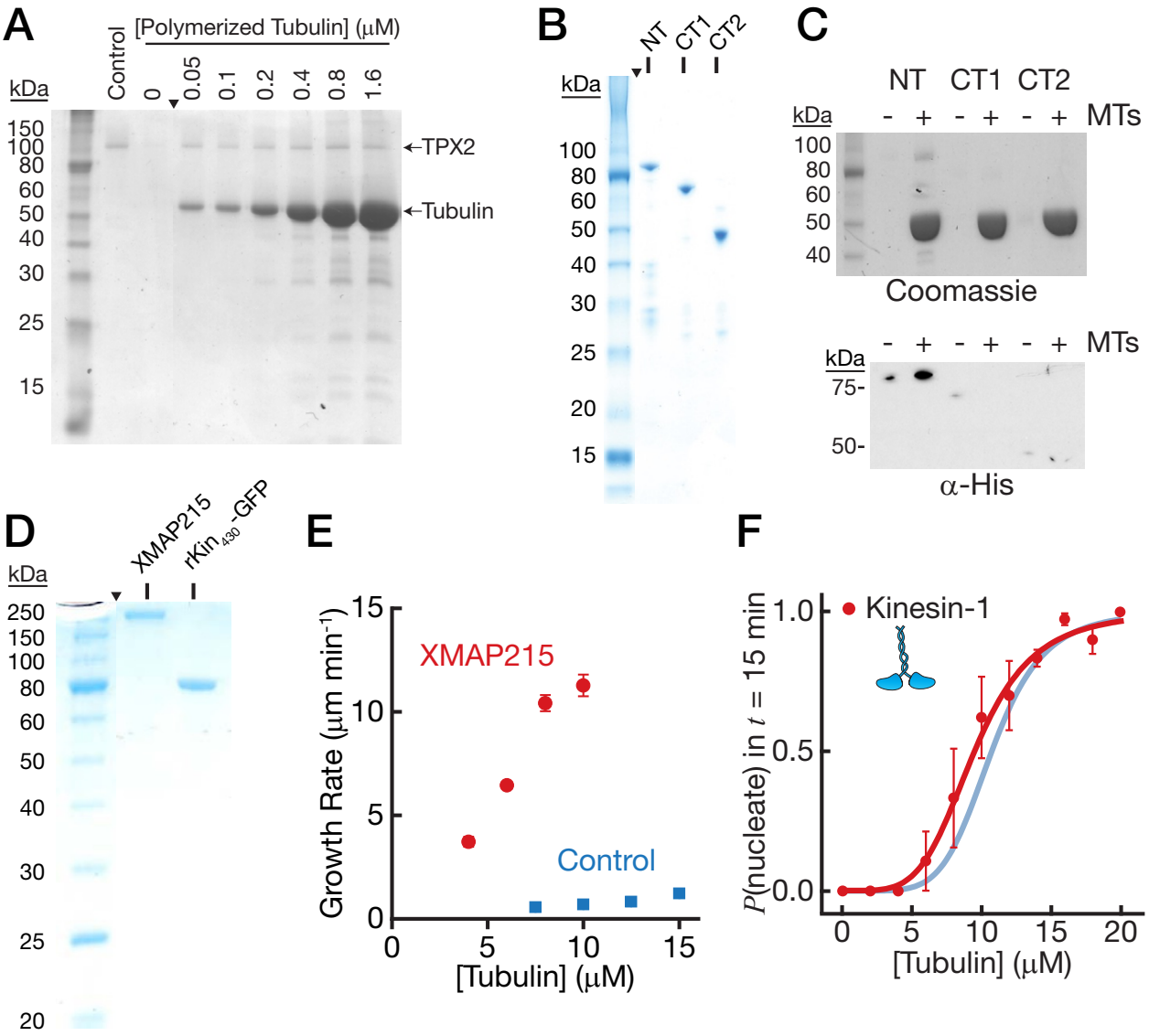

Supplementary Figure 5 Controls for the effects of TPX2, XMAP215 and GMPCPP-tubulin on nucleation in Fig. 5 & 6. **(A)** Image of a Coomassie-stained SDS-PAGE gel of a microtubule cosedimenation assay done with 200 nM TPX2. The control lane indicates a calculated amount of TPX2 that would represent 100% cosedimentation. The solid triangle points to the cropped area of the original gel provided in Supplementary Fig. 7B. **(B)** Image of a Coomassie-stained SDS-PAGE gel of the SUMO-tagged TPX2 truncation constructs NT, CT1 and CT2 expressed and purified from bacteria. The solid triangle points to the cropped area of the original gel provided in Supplementary Fig. 7C. **(C)** (*Top*) Image of a Coomassie-stained SDS-PAGE gel of a cosedimentation assay done with 200 nM of NT, CT1 or CT2 in the presence (+) and absence (-) of 1 μM taxol-stabilized microtubules. (*Bottom*) Image of a Western blot against the 6xHis-tag confirming that only NT cosediments with microtubules. **(D)** Image of a Coomassie-stained SDS-PAGE gel showing the purified protein fractions for XMAP215 and $rKin_{430}$-GFP. The solid triangle points to the cropped area of the original gel shown in Supplementary Fig. 7D. **(E)** Plot of microtubule growth rates against tubulin concentration in the presence of 200 nM XMAP215 (red) and in control buffers (blue). For increasing tubulin concentrations, $n = 3$, 29, 41 and 53 microtubules, respectively with 200 nM XMAP215 and 31, 47, 21 and 18 microtubules, respectively without XMAP215. Data were pooled across 3 experiments. Error bars represent s.e.m. **(F)** Plot of the nucleation probability in the presence of 200 nM $rKin_{430}$-GFP (kinesin-1). The solid red line is the sigmoidal equation fit. The fit from the control data is shown in light blue for comparison. For increasing tubulin concentrations, $n = 15$, 10, 10, 30, 30, 30, 30, 20 and 20 GMPCPP seeds, respectively. Data were pooled across 1-3 experiments. Error bars represent s.e.m.

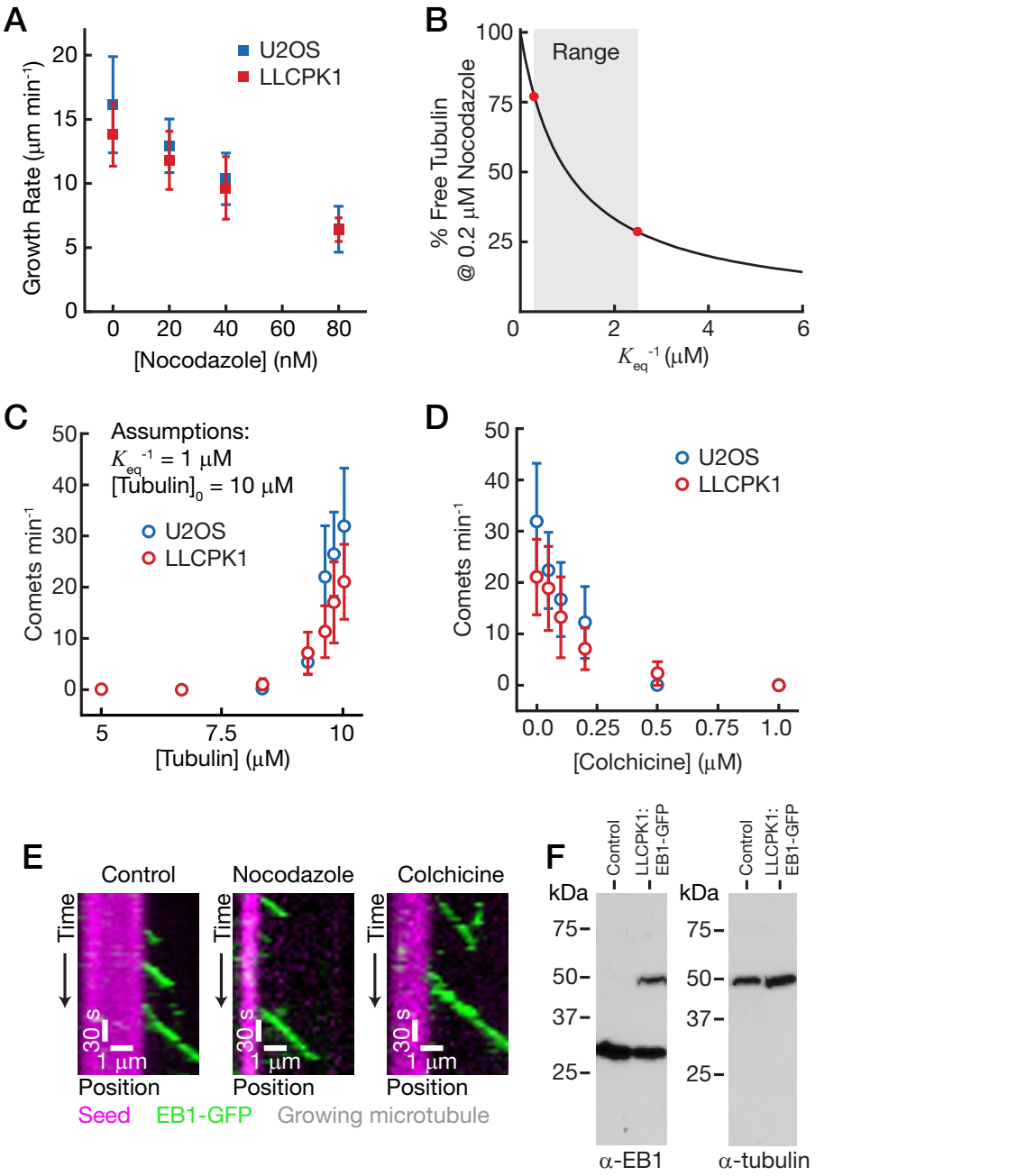

Supplementary Figure 6 Controls and model for effects of tubulin depletion by nocodazole on nucleation in cells in Fig. 7. **(A)** Plot of the microtubule growth rate against nocodazole concentration in two cell lines (U2OS, blue; LLCPK1, red). The microtubule growth rates were inferred from the velocity of EB comets. For increasing nocodazole concentrations, $n = 25$(2 independent experiments), 13(2), 13(2) and 10(2) (for LLCPK1 cells) and 20(2), 17(2), 12(2) and 12(2) (for U2OS cells) EB comets. Error bars represent the s.d. **(B)** Plot of the percentage of free soluble tubulin as a function of nocodazole concentration. Assuming a 1:1 stoichiometry and equilibrium conditions, we model the percentage of free tubulin as % Free Tubulin = 100 / (K_{eq}^{-1}[Nocodazole] + 1), where K_{eq} is the equilibrium constant. The range of measured equilibrium constants is indicated. **(C)** Theoretical plot of the centrosomal nucleation rate (comets • min^{-1} emerging from the centrosome) against predicted tubulin concentration in two cell lines (U2OS, blue; LLCPK1, red). The plot assumes an equilibrium constant for tubulin:nocodazole binding of 1 μM and a baseline soluble tubulin concentration of 10 μM. **(D)** Plot of the centrosomal nucleation rate against colchicine concentration in two cell lines (U2OS, blue; LLCPK1, red). For increasing colchicine concentrations, $n = 12$, 19, 18 and 19 U2OS cells, respectively and $n = 29$, 17, 20, 22 and 22 LLCPK1 cells, respectively. Data were pooled across 2 experiments. Error bars represent the s.d. **(E)** Kymographs of EB1-GFP end-tracking *in vitro* in control buffers (*left*), in the presence of 200 nM nocodazole (*middle*), or in the presence of 1 μM colchicine (*right*). **(F)** Images of Western blots performed against EB1 (left) and tubulin (right) on LLCPK1:EB1-GFP cells. The EB1 blot shows a band at ~55 kDa in the LLCPK1:EB1-GFP cell line that is absent in the control LLCPK1 cells. We estimate EB1-GFP overexpression at ~30% relative to the endogenous level based on the intensity of this band measured from two independent blots.

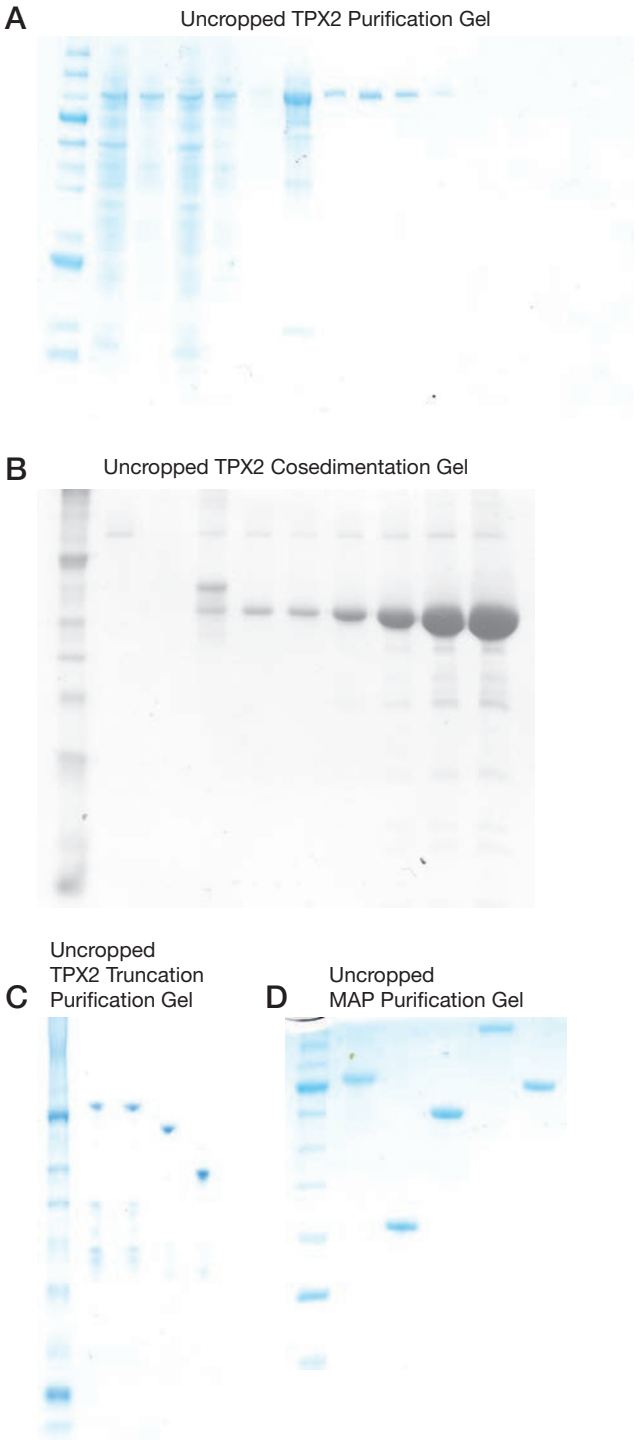

Supplementary Figure 7 Uncropped SDS-PAGE gels. **(A)** Uncropped scanned image file of the TPX2 purification SDS-PAGE gel shown in Fig. 5A. **(B)** Uncropped scanned image file of the TPX2 cosedimentation assay SDS-PAGE gel shown in Supplementary Fig. 5A. **(C)** Uncropped scanned image file of the SUMO-tagged TPX2 truncation construct purification SDS-PAGE gel shown in Supplementary Fig. 5C. **(D)** Uncropped scanned image file of the MAP purification gel shown in Supplementary Fig. 5D.

Supplementary Video Legends

Supplementary Video 1 Microtubule nucleation from GMPCPP seeds at 12 μM tubulin. Epifluorescence images of GMPCPP microtubule seeds (magenta) combined with total-internal-reflection fluorescence images of elongating microtubules (green) were recorded at 10 s intervals for 15 min. Some GMPCPP seeds are observed to produce microtubules immediately while others produce microtubules after a time lag. Some GMPCPP seeds do not produce microtubules during the experiment. Video playback is 100x real-time (see time stamp).

Supplementary Video 2 Hysteresis in microtubule elongation experiments. Epifluorescence images of GMPCPP microtubule seeds (magenta) combined with total-internal-reflection fluorescence images of elongating microtubules (green) were recorded at 10 s intervals. At the start of the experiment, the GMPCPP seeds are exposed to 4 μM tubulin (indicated). After a short period, the solution is exchanged with 15 μM tubulin (indicated). At this concentration, the GMPCPP seeds produce microtubules readily. The solution is exchanged back to 4 μM tubulin (indicated). Microtubules continue to elongate until they undergo catastrophe, after which the GMPCPP seed is dormant. Video playback is 100x real-time (see time stamp).

Supplementary Video 3 LLCPK1 cells expressing GFP-EB1. Spinning-disk confocal images of LLCPK1 cells constitutively expressing GFP-EB1. Images were taken every 2 s. Playback is 20x real-time (see time stamp).

Supplementary Video 4 LLCPK1 cells expressing GFP-EB1 in the presence of 40 nM nocodazole. Spinning-disk confocal images of LLCPK1 cells constitutively expressing GFP-EB1 in the presence of 40 nM nocodazole. Fewer “comets” emerge from the centrosome. Images were taken every 2 s. Playback is 20x real-time (see time stamp).